Acta Biochim Biophys Sin 2026, 58(9): 1988–2006
https://cstr.cn/32197.14.abbs.2026071
https://doi.org/10.3724/abbs.2026071
Original Article

Original Article

Sti1 participates in the dynamics of protein aggregation triggered by glucose signaling in *Saccharomyces cerevisiae*

Jiawei Chen[1,2], Jiayu Zhou[1,2], Keren Sun[1,2], Hanlin Zhang[1,2], Yanqiu Ji[1,2], Letong Li[1,2], Wanjie Li[1,2,*], and Fei Dou[1,2,*]

[1]Key Laboratory of Cell Proliferation and Regulation Biology, Ministry of Education, Beijing Normal University, Beijing 100875, China, and [2]College of Life Sciences, Beijing Normal University, Beijing 100875, China
*Correspondence address. E-mail: douf@bnu.edu.cn (F.D.); lwj@bnu.edu.cn (W.L.)

Received 23 October 2025 Accepted 13 April 2026 Published 30 April 2026

Abstract

Environmental changes put stress on living organisms. We find that nutrient starvation induces dynamic protein aggregations in yeast cells, and many chaperones are involved in this process. Among them, Sti1/HOP, the co-chaperone of Hsp70 and Hsp90, plays roles in the formation of protein quality control (PQC) compartments and protein stasis (or proteostasis) maintenance, and it co-localizes to insoluble protein deposits (IPOD) by liquid-liquid phase separation (LLPS). Notably, the subcellular localization and cytoplasmic aggregation of Sti1 are rigorously regulated by the PQC machinery, including Ssa1/Hsp70 and Hsp82/Hsp90. On the other hand, *STI1* deletion abolishes cytoplasmic aggregation of chaperones, including Ssa1, Hsp42, and Hsp104. These results reveal an interdependent model of chaperone-mediated aggregate formation. Furthermore, lysine 9 (K9) of Sti1 is identified as a critical residue governing its cytoplasmic condensation through a potential post-translational modification.

Key words quiescence, glucose depletion, Sti1, condensate, LLPS

Introduction

In living cells, protein homeostasis (or proteostasis) maintenance is very important, especially when cells are suffering from environmental stress (elevated temperature, nutrient depletion, *etc.*). Both newly born and mature proteins are at risk for misfolding and aggregation. The protein quality control (PQC) system monitors these inevitable mishaps and facilitates the clearance of misfolded or damaged proteins by refolding or degradation [1–4]. The PQC system primarily executes regulatory functions through three mechanisms: (1) molecular chaperones, which stabilize proteostasis, interact with client proteins to promote correct folding and assembly, and enable refolding of misfolded species [2]; (2) the ubiquitin-proteasome pathway degrades soluble misfolded proteins [5]; and (3) the autophagy-lysosome system clears insoluble protein aggregates and dysfunctional organelles (*e.g.*, mitochondria) [5]. In cells, 3 distinct types of PQC compartments mediate refolding and degradation of protein aggregates in the cytoplasm: cytoplasmic Q-bodies (CytoQs), juxtanuclear quality control (JUNQ) compartments, and insoluble protein deposits (IPODs) [6,7]. Upon stress, PQC balance is broken, and misfolded or unfolded proteins begin to accumulate. To avoid further damage, CytoQs are formed and sequestered these cytotoxic proteins/polypeptides in the cytoplasm randomly. As misfolded proteins aggregate more, these misfolded proteins/polypeptides are sorted to IPOD or JUNQ depending on their solubility. The soluble proteins assemble JUNQ near the nucleus (the corresponding compartment in the nucleus is called INQ), recruiting proteasomes to enable degradation. Accordingly, insoluble aggregates are deposited into IPOD structures adjacent to the vacuole. These compartment sorting and assembly processes are chaperone-dependent and help cells maintain proteostasis under stress [8]. Impairment or overload of PQC (*i.e.*, aging or environmental stress) can lead to the accumulation of misfolded proteins, which may contribute to neurodegenerative diseases and cancer [9].

Molecular chaperones play key roles in cellular PQC, which accompanies proteins throughout life, from synthesis to degradation. Chaperone Hsp70 and Hsp90 families are highly conserved across eukaryotes and prokaryotes, which facilitate newly born protein maturation. The client protein transfer between Hsp70 and Hsp90 depends on the co-chaperone Sti1/Hop [10,11]. Since its discovery in 1989, Sti1 has been extensively characterized structurally across mammalian systems [12]. Its protein architecture comprises three tetratricopeptide repeat (TPR) domains (TPR1,

© The Author(s) 2026. This is an open access article distributed under the terms of the Creative Commons Attribution-NonCommercial-NoDerivs License (https://creativecommons.org/licenses/by-nc-nd/4.0/).

TPR2A, and TPR2B) and two DP (domain present in Sti1) domains (DP1 and DP2) [13–15]. Structural analyses demonstrate that each TPR domain contains three tandem TPR motifs, forming conserved binding sites for Hsp70 and Hsp90 [16]. Notably, the Hsp70 C-terminal heptapeptide PTIEEVD interacts with TPR1 through high-affinity binding while engaging TPR2B via low-affinity interactions [17]. Conversely, Hsp90 C-terminal MEEVD peptide exhibits preferential binding to TPR2A [17,18]. Biophysical studies confirm that these electrostatic interactions potentiate chaperone-cochaperone complex stabilization through C-terminal-TPR domain coordination [18–21]. Functioning as a molecular scaffold mediating Hsp70-Hsp90 crosstalk, Sti1 orchestrates client protein transfer through sequential conformational transitions [10,11]. Mechanistically, Hsp70 initially engages nascent polypeptides via its substrate-binding domain in an open conformational state, facilitating proper folding while anchored to TPR1 [22]. Subsequent ATP-driven conformational changes promote client transfer to Hsp90 dimers bound to TPR2A, with final complex relocation to TPR2B [17,22]. This tripartite Hsp70-Sti1-Hsp90 system facilitates ribosomal polypeptide chain synthesis and co-translational folding through spatially coordinated interactions [23–27]. Collectively, these findings demonstrate Sti1's pivotal role in maintaining kinetic partitioning between Hsp70 and Hsp90, thereby ensuring proteostatic equilibrium under stress conditions. On the other hand, when the protein degrades, Sti1 forms a stable ternary complex with Hsp70 and Hsp90 to ensure efficient proteolysis. This complex promotes the association between the 19S regulatory particle and the 20S proteolytic core of the proteasome while also stabilizing the 26S and 30S proteasome structures through interactions with additional subunits. Mutation or deletion of the TPR domain in Sti1 disrupts this coordination, leading to the formation of a less efficient Hsp70-Hsp90 binary complex and markedly reducing both proteasome assembly and the degradation of misfolded proteins [28]. Furthermore, under environmental stress, harmful protein aggregates or stress granules (SGs) may form. Other chaperones, such as Hsp104, Hsp70, and Hsp42 in yeast, facilitate the disassembly of these aggregates for subsequent refolding. Thus, molecular chaperones and their co-chaperones play critical roles not only in the formation but also in the dissolution of protein compartments [8,29].

Recent research on intracellular protein aggregates has focused on the loss of proteostasis under various stress conditions. Intrinsic factors (genetic mutations, translational errors, or aberrant protein modifications) can lead to protein fibril tangles and contribute to neurodegenerative diseases [9,30–32]. Extrinsically, oxidative stress disrupts amino acid structures, thermal stress causes protein unfolding, and changes in pH or osmotic pressure compromise protein charge and stability [33,34]. Additionally, impaired chaperone function or decreased efficiency of protein degradation systems can also result in the accumulation of protein aggregates [35–37]. Sti1, an essential co-chaperone, undergoes stress-induced nuclear accumulation upon heat shock or hydroxyurea treatment, which is associated with cell cycle arrest [28,38,39]. In *Caenorhabditis elegans*, knockout of *STI1* attenuates the heat shock response [40]. Deletion of *STI1* in yeast compromises cellular growth under elevated temperatures and alters mitochondrial morphology, a condition that inherently promotes protein misfolding [41–43]. Furthermore, in mammalian cells, loss of *Sti1*/*Hop* function can even induce apoptosis in fibroblasts [28]. Recent evidence indicates that Sti1 participates in the formation and regulation of stress granule-like inclusions under physiological stress, which co-localize extensively with misfolded proteins [44]. Genetic ablation of *STI1* leads to the accumulation of soluble, ubiquitinated, misfolded proteins and potently activates the heat shock response [44]. Notably, its mammalian ortholog Hop undergoes phase separation with Argonaute 2 (Ago2) under stress, forming biomolecular condensates [45]. However, further details still need to be elucidated. Previous studies have found some of the trigger conditions to promote protein aggregation via overloaded PQC [8,9], but nutritional conditions, especially carbon source depletion, are seldom reported. As mentioned above, the subcellular localization of Sti1 under stress may be functionally linked to PQC components, such as Hsp70, Hsp104, and Hsp42.

In the present study, we employed *Saccharomyces cerevisiae* as a model organism to investigate the dynamic localization of some PQC markers and Sti1 under different nutrition conditions. We demonstrate the formation of protein aggregates in response to different carbon source conditions. We show that Sti1 undergoes liquid-liquid phase separation (LLPS) to form cytoplasmic condensate, which is regulated by Ssa1, Hsp82, Hsp104, and Hsp42, then establish a functional network linking Sti1 to PQC-related aggregate assembly. Furthermore, lysine 9 (K9) is identified as a critical residue governing the formation of cytoplasmic Sti1 aggregates, and post-translational modifications might be involved. Our findings establish nutrient signal-induced protein aggregates via PQC overload and reveal a Sti1-LLPS-mediated PQC network.

Materials and Methods

Yeast strains and growth conditions

S. cerevisiae strains employed in this study are listed in Supplementary Table S1. Plasmid constructions were performed using a protocol as described for pGFP-Hsp82 previously [46]. All strains were transformed from W303A by homologous recombination with linearized integration plasmids or PCR products [47–49]. The primers used to construct plasmids and homologous recombination are listed in Supplementary Table S2.

Yeast strains were grown on synthetic complete (SC) medium-plates with 0.67% yeast nitrogen base (Y8040; Solarbio, Shanghai, China), 2% glucose (G8150; Solarbio), and supplemented with appropriate amino acid dropout mix (Clontech, Beijing, China) [46]. After cultivation at 30°C for 48 h, fresh single-colony cells could be picked to GMM liquid medium (0.67% yeast nitrogen base, 2% glucose, and essential amino acids according to the strain) and incubated at 30°C and 250 rpm for 16 h or overnight [46]. Then, overnight cultures were washed twice with PBS by centrifugation and transferred to fresh GMM-glucose (0.67% yeast nitrogen base, essential amino acids according to the strain) or GMM-NH_4^+ (0.67% yeast nitrogen base without ammonium sulfate, 2% glucose, and essential amino acids according to the strain) at a final concentration of OD_{600} = 0.2 [46]. After growing at 30°C and 250 rpm for 3–5 h, fluorescence imaging was performed. Meanwhile, overnight cultures were also transferred to fresh GMM at a final concentration of OD_{600} = 0.01 to draw the growth curve and show the fluorescence localization by microscopy.

Microscopy and LLPS imaging *in vivo*

The 2-μL cultures with slides were placed on the stage and then visualized by fluorescence microscopy with 488 and 543 nm lasers

through an oil immersion 100× objective (Axio Imager 2; Zeiss, Oberkochen, Germany) during different phases [46].

For LLPS imaging of living cells, 2-μL cultures with slides were placed on the stage and then visualized by a confocal microscope (LSM 700; Zeiss) at room temperature.

Membrane staining

For quiescent cells, cultures were washed twice with PBS by centrifugation and then transferred to 100 μL PBS with 2 μL FM4-64 (T13320; 1 mg/mL; Sigma, St Louis, USA) at a final concentration of OD_{600} = 0.2–0.4. Cells were incubated at 30°C and 250 rpm for 1 h and then visualized by fluorescence microscopy through an oil immersion 100× objective.

For cells under glucose starvation, 100 μL cultures were mixed with 1 μL FM4-64 (1 mg/mL), incubated at 30°C and 250 rpm for 1 h, and then visualized by fluorescence microscopy through an oil immersion 100× objective.

Inhibition of LLPS by 1,6-hexanediol

For quiescent cells, 1,6-hexanediol (A601513; Sangon, Shanghai, China) was added to cultures with a gradient (0%, 5%, or 10%), incubated at 30°C for 30 min with shaking, and then visualized by fluorescence microscopy through an oil immersion 100× objective.

For cells under glucose starvation, 1,6-hexanediol was added to cultures with a gradient (0%, 5%, or 10%), incubated at 30°C for 3 h with shaking, and then visualized by fluorescence microscopy through an oil immersion 100× objective.

Protein purification

All purified proteins were fused with His6 by the expression vectors pRSF-His6-SUMO and pET-duet1 in *E. coli*, and then a Ni column (GE Healthcare, Bethesda, USA) was used for purification, which had been reported previously [42]. Protein expression was induced by IPTG (GF101-01; TransGen, Beijing, China) at a final concentration of 0.5 mM, and the cells were cultured at 16°C with shaking at 220 rpm for 16 h. Then, all cells were harvested and lysed with 25 mM Tris-HCl (pH 7.5). After centrifugation, the supernatant was loaded onto a Ni column and purified through the AKTA pure chromatography system (GE Healthcare). For LLPS and fluorescence recovery after photobleaching (FRAP) experiments, proteins were desalted and concentrated using Amicon® Ultra-15 tubes (Millipore, Billerica, USA).

LLPS imaging *in vitro*

For purified proteins, 10 μL protein was applied to a glass-bottom cell culture dish (80100; Nest, Wuxi, China) with a coverslip at a final concentration of 90 μM [42], which contained 25 mM Tris-HCl, pH 7.5, 4 mM DTT, gradient NaCl (0–100 mM), and visualized by confocal microscopy through an oil immersion 100× objective.

FRAP

FRAP was carried out by the module of LSM 700 confocal microscope through an oil immersion 100× objective at room temperature.

For living cells, the 2-μL cultures with a slide were placed on the stage, and time lapse and bleaching were selected. Then, regions of interest (ROIs) for bleaching were marked. The pinhole was set to 4 μm, and the 488 nm laser intensity was set to 0.8%–1% for continuous scanning. Photos were continuously taken (1 picture/50–100 ms) after bleaching with 100% laser intensity. Meanwhile, the changes in the intensity of the ROI were recorded to draw the recovery curve.

For purified proteins, 10 μL protein was applied to a glass-bottom cell culture dish with a coverslip at a final concentration of 90 μM, which contained 25 mM Tris-HCl (pH 7.5), 4 mM DTT, and 30 mM NaCl. Then, under the same conditions as the live cell experiments, FRAP was performed, and the curve was plotted.

Co-immunoprecipitation and western blot analysis

Following the construction of Myc-tagged wild-type (WT) and mutant Sti1 variants (K9A, K266A, and K9A K266A) in *S. cerevisiae*, co-immunoprecipitation (Co-IP) assays targeting GFP-tagged Ssa1/Hsp82 were conducted. Yeast cultures grown in GMM were harvested at mid-log phase (OD_{600} = 0.6–0.8) and subjected to two sequential washes with ice-cold distilled deionized water (ddH_2O). Cell lysates were prepared by mechanical disruption using 425–600-μm acid-washed glass beads (G8772; Sigma) in IP lysis buffer (Applygen C1050; 50 mM Tris-HCl, pH 7.4, 150 mM NaCl, and 1% NP-40) supplemented with complete™ protease inhibitor cocktail (11873580001; Roche, Basel, Switzerland), employing a Bead Ruptor 24 homogenizer (Omni International, Kennesaw, USA) at 4°C (6 × 30 s pulses, 5 m/s). Clarified supernatants were obtained by centrifugation at 12,000 *g* for 3 min at 4°C and quantified via Bradford assay (5000006; Bio-Rad, Hercules, USA). Lysates (500 μg total protein) were incubated with anti-GFP magnetic agarose beads (SM038005; Smart-Lifesciences, Changzhou, China) for 2 h at 25°C with gentle rotation. Bead-bound complexes were washed four times with lysis buffer, and the remaining steps followed the protocol. Immunoprecipitates were visualized by western blot analysis to show the interaction between Ssa1/Hsp82 and Sti1 (WT, K9A, K266A, and K9A K266A). For reciprocal Co-IP, anti-Myc magnetic beads (P2183S; Beyotime, Shanghai, China) replaced the GFP-specific matrix. Normal mouse IgG-coupled beads (AF0031; Beyotime) served as negative controls.

Western blot analysis was performed using standardized protocols. Protein lysates were resolved on 10% SDS-PAGE gels at 100 V for 90 min. Following electrophoresis, proteins were transferred to 0.45-μm PVDF membranes (IPFL00010; Millipore). Membranes were blocked with 5% non-fat milk (232100; BD Biosciences, San Diego, USA) in TBST (50 mM Tris-HCl, 150 mM NaCl, and 0.1% Tween-20, pH 7.6) and then probed overnight at 4°C with primary antibodies diluted in blocking buffer, followed by incubation with proper HRP-conjugated secondary antibody. Immunoreactive bands were visualized using Immobilon ECL Ultra (2326801; Millipore) and quantified via a ChemiDoc Touch Imaging System (12003153; Bio-Rad).

Expected molecular masses: Myc-Sti1 (70–100 kDa, resulting from post-translational modifications), GFP-Ssa1 (~120 kDa, GFP fusion + Ssa1 core), and GFP-Hsp82 (~130 kDa, Hsp82 dimeric form). PageRuler 26616 (Thermo Scientific, Waltham, USA) served as molecular weight markers.

The primary antibodies are shown as follows: α-GFP (mouse monoclonal; KM8009; 1:5000; Sungene Biotech, Tianjin, China) and α-Myc (mouse monoclonal; M4439; 1:5000; Sigma). HRP-conjugated goat anti-mouse IgG (BE0102; 1:10,000; Easybio, Beijing, China) was used as the secondary antibody.

Gene Ontology functional enrichment analysis using Metascape

GO enrichment analysis on the target gene set was performed using

the Metascape online platform (http://metascape.org). The analysis was carried out for yeast (*S. cerevisiae*), and all genes were represented by their official gene symbols. The gene list was pasted as plain text into the input box, with *S. cerevisiae* selected as both the input and analysis species. To avoid the default express analysis, which combines multiple databases, we chose the custom analysis mode. In the enrichment tab, only the three GO sub-ontologies—biological process (GO_BP), cellular component (GO_CC), and molecular function (GO_MF)—were selected. The "Pick selective GO clusters" option was enabled to perform hierarchical clustering of redundant GO terms based on the Kappa statistic; within each cluster, only the term with the smallest *P*-value was retained as the representative for display in the main figures, thereby reducing redundancy. The background set was kept as the platform's default whole-genome annotation. Enrichment significance was calculated using the cumulative hypergeometric test (equivalent to Fisher's exact test), and a threshold of $P < 0.01$ was used to define statistically significant enrichment. After the analysis, complete results were downloaded as Excel files from the "Analysis Report Page", including GO term ID, description, enrichment factor, *P*-value, Benjamini-Hochberg corrected *q*-value, and the list of enriched genes. Visualization included bar plots [with –log10(p) on the x-axis], heatmaps, and network diagrams; in the bar plots, color intensity reflects the significance level. This approach ensures the reproducibility and interpretability of the GO analysis.

Statistical analysis

Experiments in this study were all repeated three or more times independently with similar results. The localization and bleaching shown in the microscopy, LLPS imaging, PCC and FRAP were the single biological results ($n \geq 3$), which were the average of those replicates. Growth curves and recovery curves were generated by GraphPad Prism 9 (GraphPad Software, San Diego, USA), and the standard deviations are shown by error bars. Statistical analysis was performed using a two-tailed unpaired *t* test. $P < 0.05$ was considered as significantly different.

Results

Nutrient signals promote specific molecular chaperones localized to protein aggregates

Chaperones are considered to facilitate client protein folding and maturation under normal conditions. Under stress, proteins might denature/misfold and aggregate into inclusions. Under this condition, chaperones could contribute to the formation of distinct inclusions. Temperature is a well-established stressor. Notably, it has been reported that supplementing ATP to quiescent yeast cells induces the disassembly of functional Hsp104 aggregates, indicating that nutrient deprivation might trigger protein aggregation, as does elevated temperature [29]. Many chaperones, including Hsp42 and Ssa1/Hsp70, participate in PQC processes during carbon starvation [29]. We chose several key markers to check whether glucose deprivation induces protein aggregation (Supplementary Box 1). To monitor their localization dynamics, we endogenously tagged the N- or C-terminus of each protein with GFP or mCherry via homologous recombination in yeast and observed their distribution during different growth phases in GMM medium.

We compared the localization of labeled PQC proteins in logarithmic and stationary phase cells and observed that Hsp42 was uniformly distributed in the nucleoplasm during the logarithmic phase, while Hsp104 exhibited distinct aggregation (Figure 1A). Based on previous reports, these aggregates likely represent perinuclear condensates resulting from the nutrient-limited GMM medium. In the stationary phase, cells formed prominent perinuclear compartments (with minor Hsp104 present) and cytoplasmic aggregations (where Hsp42 and Hsp104 were predominantly localized) (Figure 1B), indicating that nutrient signaling influenced the formation of misfolded protein aggregates. We also labeled the co-chaperone Sti1, which facilitates client protein folding in cooperation with Hsp70 and Hsp90. Imaging and quantitative analysis revealed that both Ssa1 and Sti1 formed aggregates in the perinuclear region and cytoplasm during the stationary phase (Figure 1B,C,E and Supplementary Figure S1). At 72 h and 48 h of stationary phase, Sti1 formed cytoplasmic and perinuclear aggregates in 87.50% ± 1.95% and 7.24% ± 0.37% of cells, respectively (mean ± SD) (Figure 1D). Under the same 72 h stationary phase condition, Ssa1 assembled into cytoplasmic and perinuclear aggregates in 82.83% ± 2.25% of cells (mean ± SD) (Figure 1D). Notably, Sti1 showed co-localization with Hsp104- and Hsp42-positive aggregates, suggesting that Ssa1/Sti1 participated in the formation of nutrient stress-induced intracellular aggregates (Figure 1B,C and Supplementary Table S3).

Protein aggregates form in distinct patterns

Since nutrient depletion could promote protein aggregation, we sought to investigate this phenomenon in more detail. First, log-phase cells were transferred into carbon- or nitrogen-deficient media, and chaperone localization was observed. Ssa1 and Sti1 formed cytoplasmic punctate aggregates under carbon starvation, while Hsp82 formed nuclear aggregates exclusively, as reported in previous research (Supplementary Figure S1) [46,50]. Notably, Hsp104 and Hsp42 also formed similar punctate structures that partially co-localized with Sti1 (Figure 1F and Supplementary Figure S1), with Pearson correlation coefficients (PCCs) of 0.77 ± 0.09 (Hsp104), 0.78 ± 0.12 (Hsp42), and 0.78 ± 0.16 (Ssa1), respectively (mean ± SD). As reported previously, some punctate cellular structures, such as stress granules (SGs) and P-bodies, are formed in the cytoplasm under normal or stress conditions. Then, we performed co-localization analysis and confirmed that Sti1 puncta partially co-localized with SGs marked by Pab1 (Figure 2 and Supplementary Figure S1E), with a PCC of 0.70 ± 0.08 (mean ± SD). It seemed that Sti1 participated in several cytoplasmic aggregates, such as CytoQ (Hsp42) and SGs (Pab1).

Now that nutrient signaling induces the aggregation of Sti1 and Ssa1 and participates in protein aggregation, we sought to investigate how prolonged nutrient depletion drives the accumulation of misfolded protein aggregates. Using time-course analysis, we monitored the localization dynamics of Sti1 and Ssa1 over an extended period. We found that both Ssa1 and Sti1 initially formed perinuclear aggregates, which were subsequently followed by the appearance of more intense fluorescent foci in the cytoplasm. Notably, Ssa1 exhibited earlier aggregation than Sti1, suggesting that Ssa1 might play a fundamental role in this process (Supplementary Figure S2).

Considering that Sti1 and other proteins could form punctate aggregates upon rapid glucose deprivation, we hypothesized that the aggregates that appeared in long-term-cultured cells might also be related to carbon source starvation. To test this hypothesis, we

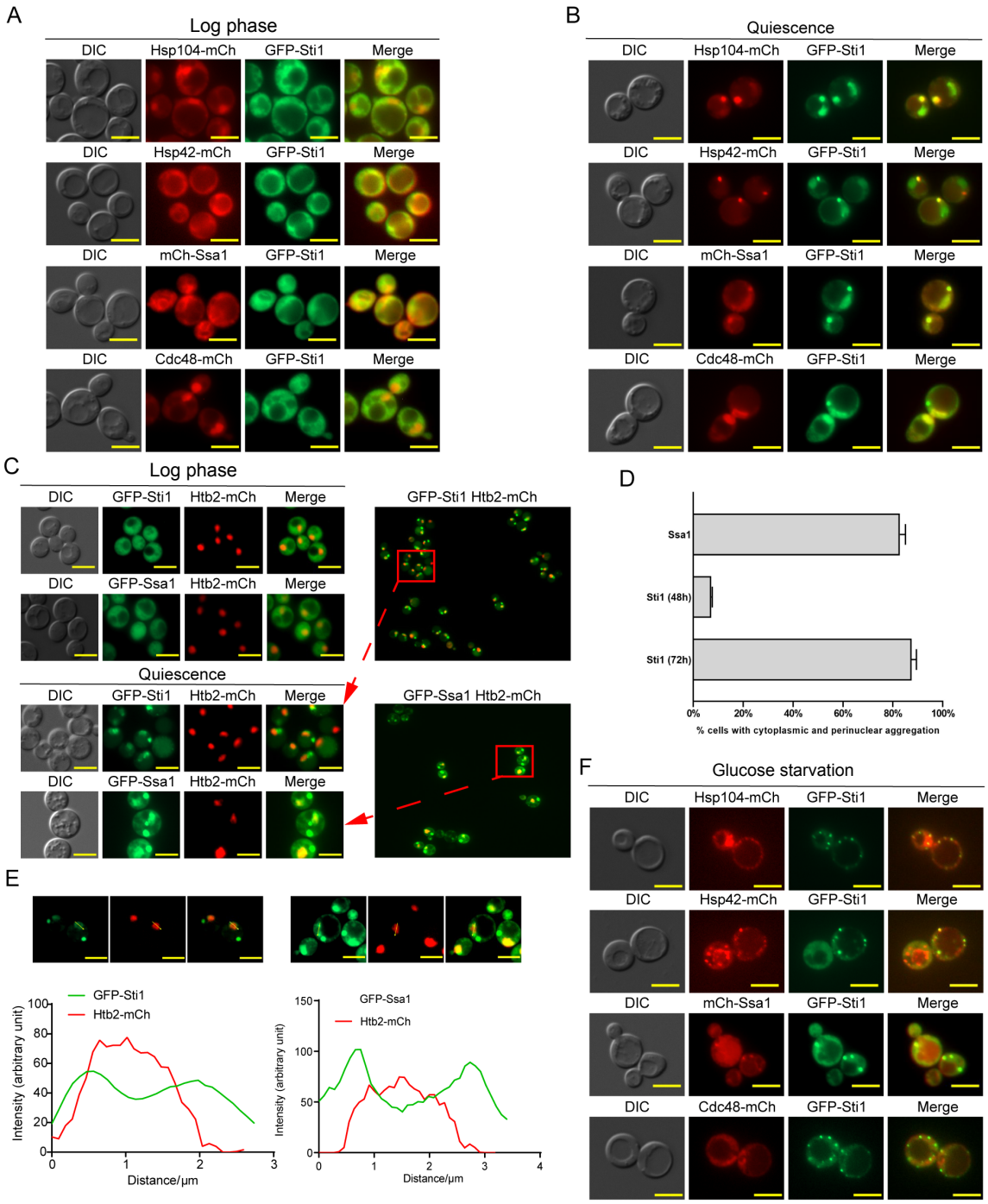


Figure 1. Nutrient signals promote specific molecular chaperones localized to protein aggregates (A) Representative fluorescence images of Sti1 co-localization with PQC components in the logarithmic phase (Hsp104 labeling JUNQ/IPOD, Hsp42 labeling IPOD, Ssa1 labeling SGs, Cdc48 indicating JUNQ position). Scale bar: 5 μm. (B) Representative fluorescence images of Sti1 co-localization with PQC components in the stationary phase. Sti1 co-localized with Hsp104 and Ssa1 in both cytoplasmic and perinuclear aggregates, with Hsp42 in cytoplasmic aggregates, and with Cdc48 (JUNQ) in perinuclear aggregates. Scale bar: 5 μm. (C) The subcellular distribution of GFP-Sti1 and GFP-Ssa1 across growth phases. Both proteins exhibited whole-cell distribution (excluding vacuoles) during the logarithmic phase, and formed cytoplasmic and perinuclear aggregates in the stationary phase. The nucleus was labeled with mCherry-tagged histone Htb2. Scale bar: 5 μm. (D) Percentage of yeast cells exhibiting cytoplasmic and perinuclear aggregates during the stationary phase. At 72 h and 48 h of stationary phase, Sti1 formed cytoplasmic and perinuclear aggregates in 87.50% ± 1.95% and 7.24% ± 0.37% of cells, respectively. At 72 h of stationary phase condition, Ssa1 assembled into cytoplasmic and perinuclear aggregates in 82.83% ± 2.25% of cells (mean ± SD). Error bars represent the SD of the mean (n = 3) for each assay. For each independent replicate, at least 100 cells were quantified. (E) Co-localization analysis between GFP-Sti1/GFP-Ssa1 and mCherry-tagged nuclear marker in the quiescence of one cell, measured by a yellow straight-line segment across the nucleus in ImageJ software. Scale bar: 5 μm. (F) Representative fluorescence images of Sti1 co-localization with PQC members under rapid glucose deprivation. Sti1 co-localized with Hsp104, Hsp42, and Ssa1 in cytoplasmic aggregates. Scale bar: 5 μm.

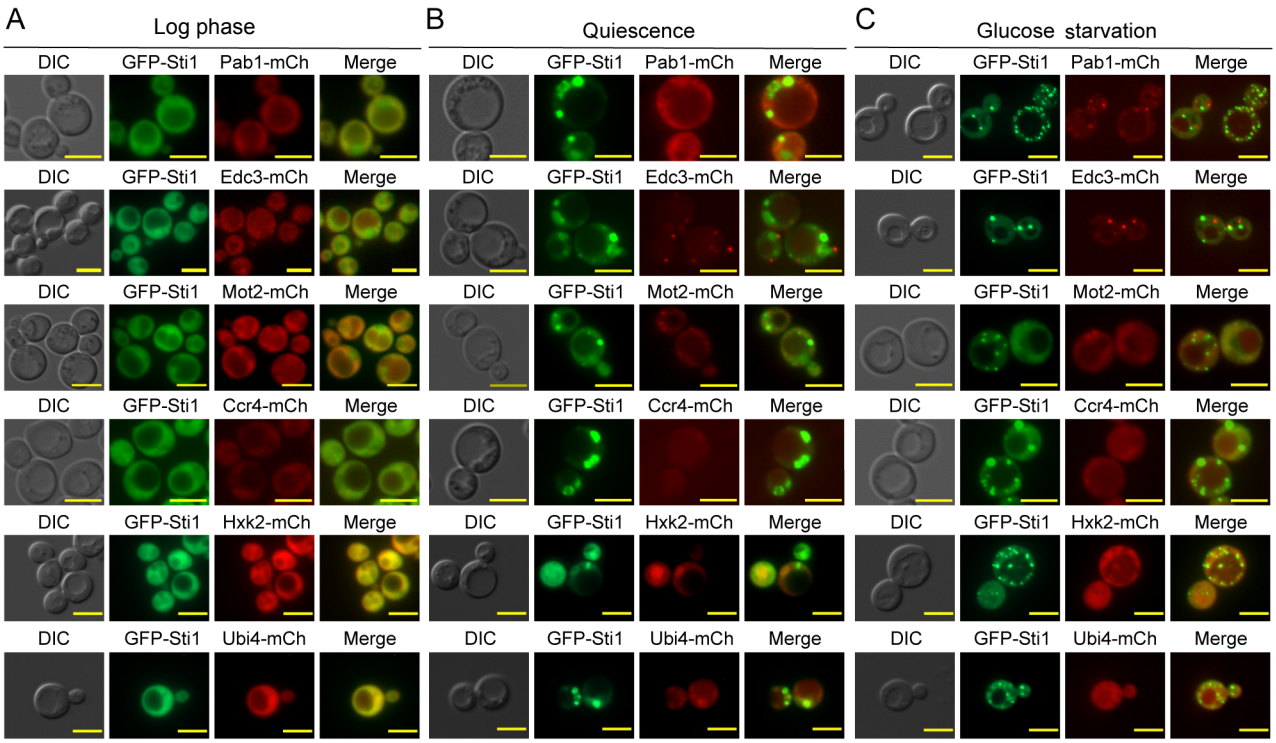


Figure 2. Protein aggregates form in distinct patterns (A) Representative fluorescence images of Sti1 co-localization with stress-responsive proteins (Pab1, Edc3, Mot2, Ccr4-Not complex, Hxk2, and Ubi4) in the logarithmic phase. All proteins exhibited whole-cell distribution (excluding vacuoles). Scale bar: 5 μm. (B) Representative fluorescence images of Sti1 co-localization with stress-responsive proteins in the stationary phase. Sti1 exhibited weak co-localization with other proteins. Scale bar: 5 μm. (C) Representative fluorescence images of Sti1 co-localization with stress-responsive proteins under rapid glucose deprivation. Partial co-localization was observed between Sti1 and Pab1. Scale bar: 5 μm.

supplemented stationary-phase cells, in which cytoplasmic aggregation had already formed, with 2% glucose (final concentration). This treatment disassembled the aggregates quickly, such that cytoplasmic Sti1 aggregates dissipated within 30 min (following glucose replenishment for 30 min, Sti1 cytoplasmic aggregates were present in 11.80% ± 1.70% of cells, mean ± SD), and perinuclear Sti1 aggregates disassembled within 3 h (following glucose replenishment for 3 h, Sti1 perinuclear aggregates were present in 2.62% ± 1.06% of cells, mean ± SD) (Figure 3A,C). While supplementation with YNB alone could not dissemble the aggregates (following YNB replenishment for 3 h, Sti1 cytoplasmic and perinuclear aggregates were present in 85.65% ± 4.07% of cells, mean ± SD) (Figure 3A,C). Meanwhile, both cytoplasmic and perinuclear Ssa1 aggregates dissolved within 3 h after glucose addition (following glucose or YNB replenishment for 3 h, Ssa1 exhibited cytoplasmic and perinuclear aggregates in 6.19% ± 1.56% and 81.57% ± 2.69% of cells, respectively, mean ± SD) (Figure 3B,C). These results showed that glucose signals regulated the protein aggregation dynamics and indicated the difference between Sti1 and Ssa1 in the glucose signal response.

Distinct biophysical properties of Sti1/Ssa1 from the PQC compartments

The PQC compartments show diverse physical characteristics. The JUNQ exhibits some mobility, while the IPOD displays insoluble behavior [6]. Consequently, fluorescence loss in photobleaching experiments typically reveal a more pronounced fluorescence reduction in JUNQ than in IPOD when bleaching cytoplasmic non-aggregated regions [6]. To further characterize the dynamic properties of Sti1 and Ssa1 aggregates under various conditions, we performed FRAP. Notably, cytoplasmic aggregates of Sti1 and Ssa1 showed significant fluorescence recovery within 300 and 400 s, respectively, while perinuclear signals exhibited no detectable recovery (Figure 4A,B, Supplementary Figure S3A, and Supplementary Videos S1–S3). Although Sti1/Ssa1 co-localized with IPOD (Hsp42 and Hsp104) and JUNQ (Hsp104 and Cdc48), their behaviors appeared distinct. We speculated that Sti1/Ssa1 might be in liquid-liquid phase separation mode on the surface of IPOD. While it was seemingly contradictory to earlier reports, we proposed that within IPOD-like assemblies—where misfolded proteins formed a dense, stable core—chaperones such as Ssa1 and Sti1 might remain dynamically active at the periphery, thereby enabling recovery after photobleaching. The limited mobility observed in perinuclear regions might result from structural constraints imposed by the endoplasmic reticulum and nuclear membrane.

To confirm this hypothesis, we first employed FM4-64 staining to check whether the Sti1/Ssa1 condensates are membraneless. As expected, cytoplasmic Sti1/Ssa1 condensates and FM4-64-stained membrane structures were clearly spatially separated (Figure 4C and Supplementary Figure S3B). Next, we treated these cells with a gradient of 1,6-hexanediol (0%, 5% or 10%; v/v), the phase separation disruptor. Cytoplasmic and perinuclear Sti1/Ssa1 aggregates responded differently. The cytoplasmic aggregates exhibited dose-dependent dissolution, whereas the perinuclear structures remained intact (Figure 4D and Supplementary Figure S3C). Under

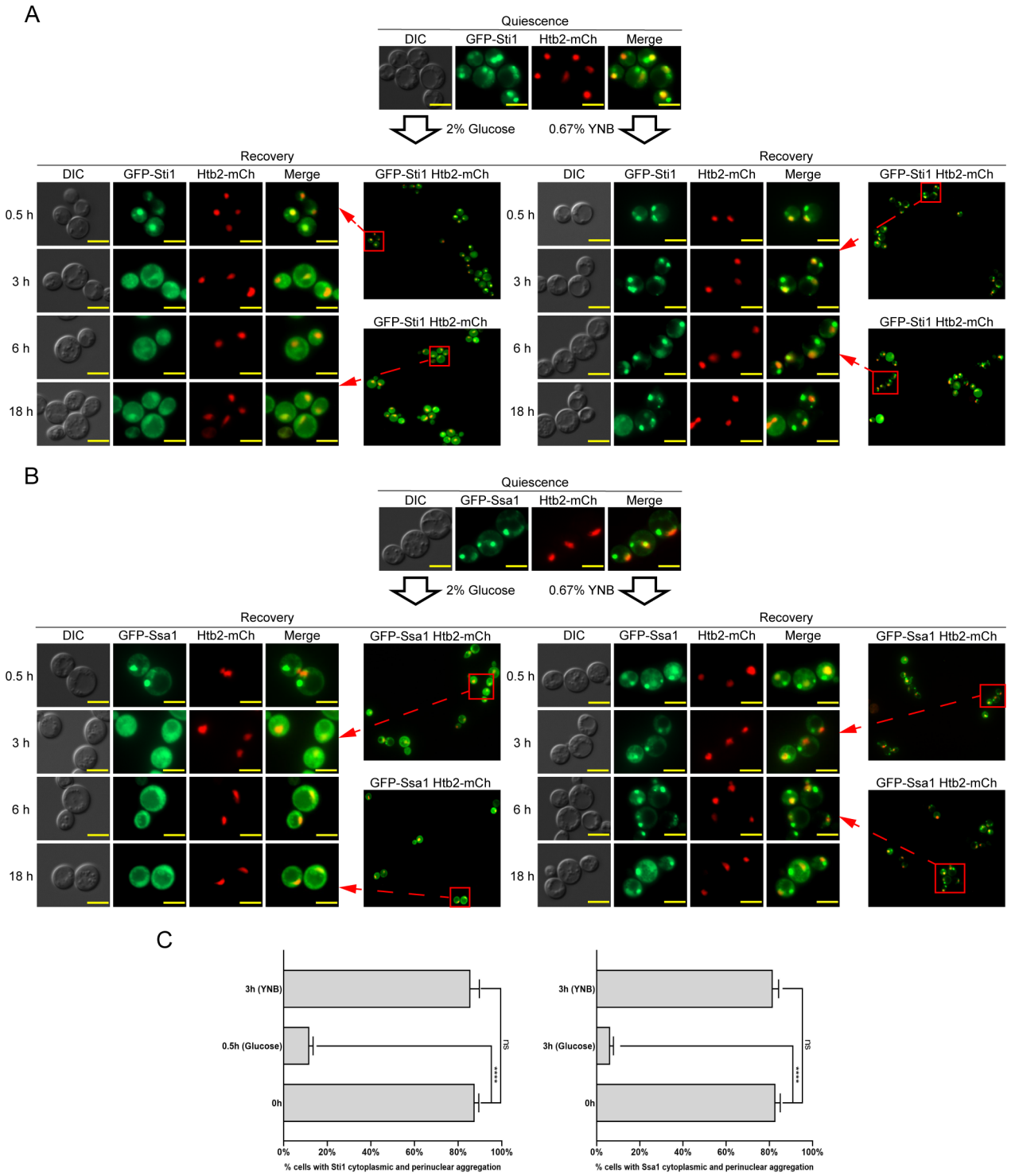


Figure 3. Relocalization of GFP-Sti1 and GFP-Ssa1 upon nutrient replenishment in stationary-phase cultures (A,B) Supplementation of 2% glucose (but not YNB) to 72-h cultures triggered rapid dissolution of Sti1 cytoplasmic aggregates within 30 min and perinuclear aggregates within 3 h. Similarly, both cytoplasmic and perinuclear Ssa1 aggregates dissipated within 3 h after glucose addition, whereas no such effect was observed with YNB supplementation. Scale bar: 5 μm. (C) Percentage of yeast cells exhibiting cytoplasmic and perinuclear aggregates during nutrient replenishment, and correlation analysis. Following glucose replenishment for 30 min, Sti1 cytoplasmic aggregates were present in 11.80% ± 1.70% of cells (mean ± SD). Following YNB replenishment for 3 h, Sti1 cytoplasmic and perinuclear aggregates were present in 85.65% ± 4.07% of cells (mean ± SD). Following glucose or YNB replenishment for 3 h, Ssa1 exhibited cytoplasmic and perinuclear aggregates in 6.19% ± 1.56% and 81.57% ± 2.69% of cells, respectively (mean ± SD). Error bars represent the SD of the mean ($n = 3$) for each assay. For each independent replicate, at least 100 cells were quantified. Statistical analysis was performed using a two-tailed unpaired *t* test (ns, not significant. ****$P < 0.0001$).

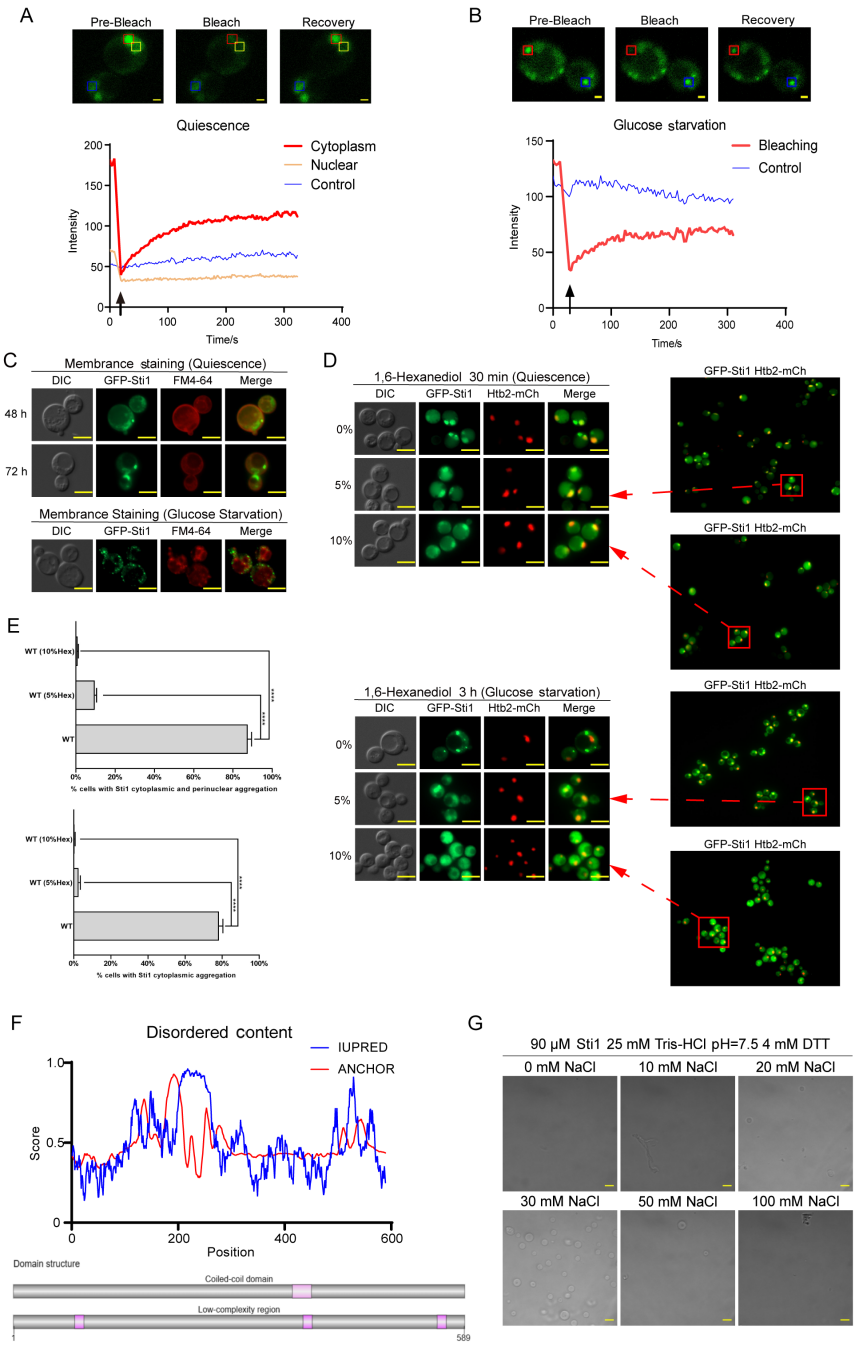


Figure 4. Sti1 forms cytoplasmic aggregates via phase separation (A,B) FRAP analysis revealed compartment-specific dynamics. Cytoplasmic condensates exhibited recovery, whereas perinuclear structures showed no fluorescence restoration within 300 s. The graph below shows the recovery as a function of time. The data are one of the independent replicates ($n \geq 3$). Scale bar: 1 μm. (C) The membrane staining of Sti1 condensates was validated by FM4-64 staining under both quiescent and glucose-deprivation conditions. Cytoplasmic condensates showed no co-localization, whereas perinuclear assemblies exhibited significant membrane adjacency. Scale bar: 5 μm. (D) Phase separation sensitivity to 1,6-hexanediol (0%, 5%, or 10%) was quantified. Cytoplasmic condensates underwent concentration-dependent dissolution (5%: dispersion; 10%: loss), in contrast to persistent perinuclear structures. Scale bar: 5 μm. (E) Percentage of yeast cells exhibiting cytoplasmic and perinuclear Sti1 aggregates under various treatments (5% hexanediol, 10% hexanediol) at 72 h of stationary phase and during rapid glucose deprivation, and correlation analysis of these percentages relative to the WT control. Under 5% 1,6-hexanediol treatment, Sti1 retained cytoplasmic aggregates in 9.61% ± 0.92% of cells during the stationary phase and in 2.56% ± 0.97% of cells under rapid glucose deprivation (mean ± SD). Under 10% 1,6-hexanediol treatment, Sti1 retained cytoplasmic aggregates in 0.84% ± 0.39% of stationary-phase cells and in 0.39% ± 0.34% of cells under rapid glucose deprivation (mean ± SD). (F) Computational prediction of Sti1 structural features. IUPRED/ANCHOR analysis identified intrinsically disordered regions (IDRs; probability score > 0.8), and DrLLPS predicted three conserved low-complexity (LC) domains. (G) Phase separation was characterized by DIC microscopy. Optimal droplet formation occurred at 20–50 mM NaCl. Scale bar: 5 μm. Error bars represent the SD of the mean (n = 3) for each assay. For each independent replicate, at least 100 cells were quantified. Statistical analysis was performed using a two-tailed unpaired t test (****$P < 0.0001$).

5% hexanediol treatment, Sti1 retained cytoplasmic aggregates in 9.61% ± 0.92% of cells during the stationary phase and in 2.56% ± 0.97% of cells under rapid glucose deprivation, while Ssa1 retained cytoplasmic aggregates in 22.69% ± 3.56% of stationary-phase cells (mean ± SD) (Figure 4E and Supplementary Figure S3D). In the presence of 10% hexanediol, Sti1 retained cytoplasmic aggregates in 0.84% ± 0.39% of stationary-phase cells and in 0.39% ± 0.34% of cells under rapid glucose deprivation, whereas Ssa1 retained cytoplasmic aggregates in 6.60% ± 1.14% of stationary-phase cells (mean ± SD) (Figure 4E and Supplementary Figure S3D). Above all, the cytoplasmic Sti1/Ssa1 aggregates were driven by LLPS.

Sti1 exhibits phase separation capability *in vitro*

Although intracellular observations have established the capacity of Sti1 for phase separation, its intrinsic LLPS propensity remains uncharacterized. First, we predicted Sti1 and Ssa1 phase separation propensity using the DrLLPS (Liquid-Liquid Phase Separation Database) and CD-CODE (Composition-Dependent Predictor) algorithms. These analyses predicted structural features, including (1) intrinsically disordered regions (IDRs) and (2) a C-terminal low-complexity domain (LCD), both of which are hallmarks associated with phase separation (Figure 4F and Supplementary Figure S3E). Then, we purified recombinant Sti1 and Ssa1 from *E. coli* (Supplementary Figure S4A,B) and assessed their LLPS capability under varying ionic concentrations (0–100 mM NaCl, and 25 mM Tris-HCl, pH 7.5) using DIC microscopy. Sti1 underwent spontaneous LLPS within the range of 20–50 mM NaCl, forming protein droplets in a concentration-dependent manner (Figure 4G). In contrast, Ssa1 exhibited little phase separation capability, with sparse droplets observed only at 30 mM NaCl (Supplementary Figure S3F). FRAP experiments using an EGFP-Sti1 fusion protein demonstrated dynamic fluidity within Sti1 condensates, with fluorescence recovery occurring within 150 s (Supplementary Figure S4C,D and Supplementary Video S4). Then, we deleted three predicted LLPS-key sequences of Sti1 and found that every deletion abolished its phase separation capacity (Supplementary Figure S5A–C). Together, these *in vitro* analyses demonstrated that Sti1 possessed an intrinsic LLPS capability, mediated by all its IDRs and LCD, which drove the biogenesis of cytoplasmic protein aggregates *in vivo*.

Sti1 phase separation *in vivo* depends on the chaperone system

As in previous results, there was a spatial correlation between Sti1 and Ssa1 upon glucose deprivation. The *in vitro* reconstitution of Sti1 phase separation required stringent physicochemical conditions, so it was likely that additional auxiliary regulators contribute to Sti1 condensate formation [51]. Notably, although Hsp82 and Sti1 did not co-localize in the cytoplasm during the stationary phase, there was an interaction between them when cells grew in a nutrient-rich environment. As a well-known co-chaperone of Hsp82, Sti1 condensate formation might be regulated by Hsp82. Accordingly, we proposed that both Ssa1 and Hsp82 probably play potential roles in this process.

To confirm whether Ssa1 and/or Hsp82 play regulatory roles in Sti1 condensation, we deleted *SSA1* or *HSP82* in a GFP-Sti1 yeast strain and examined its subcellular localization across different growth phases. Subcellular localization analysis revealed that during the logarithmic phase, GFP-Sti1 exhibited a whole-cell distribution (excluding vacuoles) in every strain (Figure 5A). However, its localization in the stationary phase diverged from that of WT: (1) in both *ssa1*Δ and *hsp82*Δ mutants, GFP-Sti1 formed intense perinuclear aggregates at 48 h, which transitioned into diffuse perinuclear accumulation by 72 h (Figure 5B,D); and (2) under rapid glucose deprivation, these mutants also showed a reduced density of cytoplasmic condensates (Figure 5F). Specifically, in the *ssa1*Δ strain, Sti1 retained a dual-focus localization in 1.35% ± 0.52% of cells at 48 h and 2.76% ± 1.06% at 72 h (mean ± SD) (Figure 5C,E). Correspondingly, in the *hsp82*Δ strain, Sti1 maintained this dual-focus pattern in 1.43% ± 0.25% of cells at 48 h and 2.57% ± 0.44% at 72 h (mean ± SD) (Figure 5C,E). Under conditions of rapid glucose deprivation, Sti1 retained a wild-type-like localization pattern in 8.88% ± 0.16% of cells in the *ssa1*Δ strain and 8.47% ± 0.16% of cells in the *hsp82*Δ strain (mean ± SD) (Figure 5G). These findings suggested that deletion of *SSA1* or *HSP82* impaired the ability of Sti1 to undergo cytoplasmic phase separation under these conditions, although it did not abolish perinuclear aggregation. The order of chaperone system assembly in the perinuclear and cytoplasmic regions indicated that aggregates were redirected to cytoplasmic sites such as the IPOD near the vacuolar PAS when the refolding capacity of chaperones and/or the degradation capacity of the proteasome were exceeded. Collectively, these data indicated that Ssa1 and Hsp82 acted as potential regulators of Sti1 condensate formation.

Furthermore, based on the established functional link between Sti1 and the PQC machinery, we generated knockout strains of *HSP104* or *HSP42* in the GFP-Sti1 background and analyzed the subcellular localization of Sti1 across growth phases. Notably, the localization pattern closely mirrored that observed in *SSA1* or *HSP82* deletion mutants (Supplementary Figure S6). Specifically, in the *hsp104*Δ strain, Sti1 retained a dual-focus localization in 1.64% ± 0.73% of cells at 48 h and 2.19% ± 0.69% at 72 h (mean ± SD) (Figure 5C,E). Correspondingly, in the *hsp42*Δ strain, Sti1 maintained a dual-focus pattern in 2.38% ± 0.30% of cells at 48 h and 2.11% ± 1.08% at 72 h (mean ± SD) (Figure 5C,E). Under conditions of rapid glucose deprivation, Sti1 retained a WT-like localization pattern in 7.97% ± 0.89% of cells in the *hsp104*Δ strain and 9.61% ± 0.50% of cells in the *hsp42*Δ strain (mean ± SD) (Figure 5G). These results demonstrated that the phase separation of Sti1 *in vivo* also depends on Hsp104 and Hsp42.

Sti1 lysine 9 (K9) is a critical residue regulating its involvement in aggregate formation and its capacity for phase separation

Our findings demonstrated that Ssa1 and Hsp82 are essential regulators of Sti1 aggregate formation at the cellular level. As a central adaptor bridging Hsp70 and Hsp90 in yeast, Sti1 maintains proteostasis through the assembly of a dynamic ternary complex (Hsp90 dimer-Sti1-Hsp70). In mammalian cells, the key residues of Sti1 for Hsp70/Hsp90 binding were reported: K8 engages Hsp70 via electrostatic interactions, while K228 anchors to Hsp90 through a hydrophobic pocket [28]. Mutational analyses indicated that the K8A/K228A double mutation in Sti1 reduces chaperone binding affinity and disrupts protein aggregate formation [28]. Thus, we proposed that these lysine residues are deterministic for Sti1 phase separation and subsequent condensate assembly.

Do these two residues serve as critical binding regions for chaperones in yeast? We performed cross-species structural

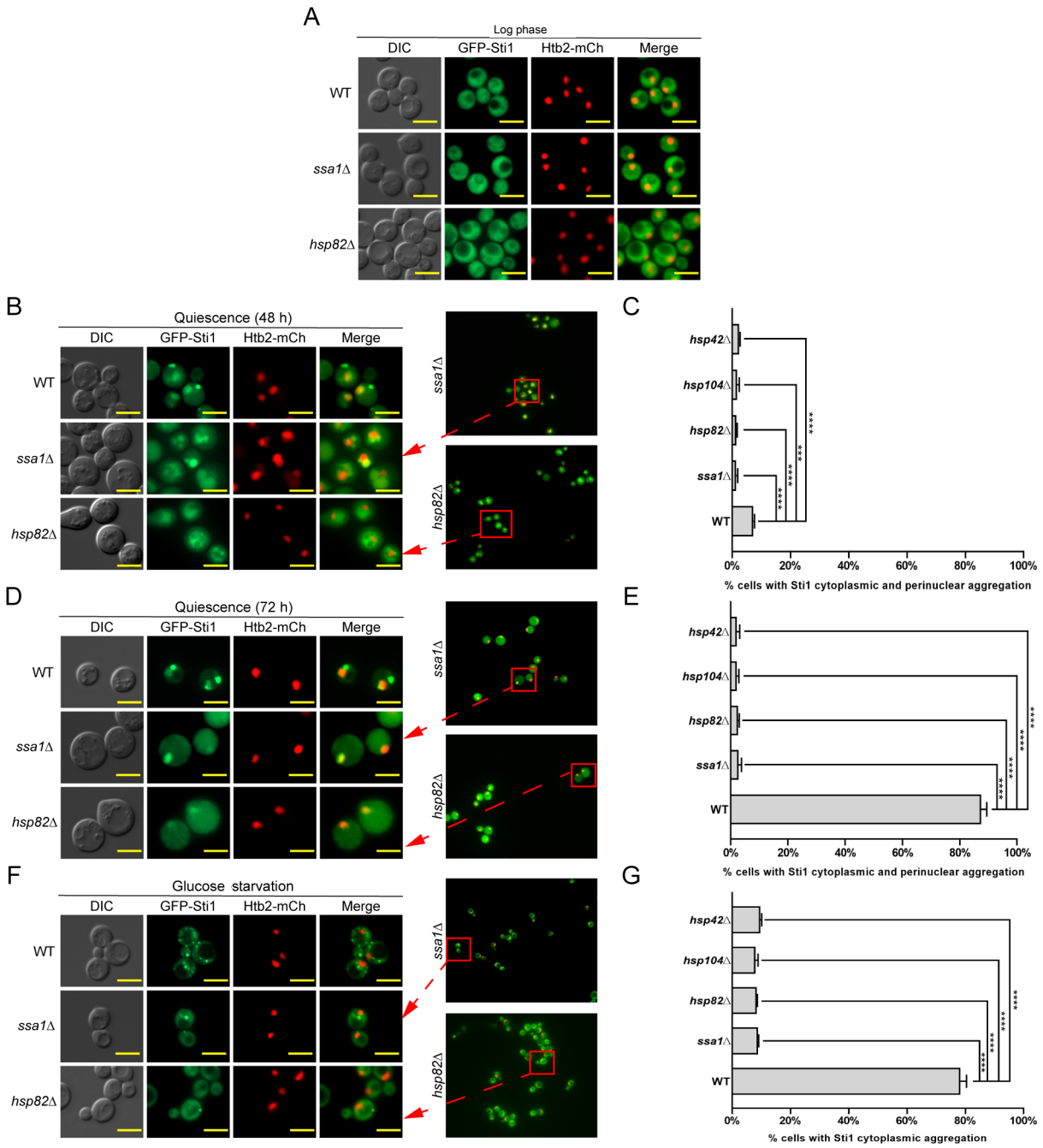


Figure 5. Sti1 phase separation *in vivo* depends on the chaperone system (Ssa1/Hsp82) (A) The subcellular distribution of GFP-Sti1 in various strains (WT, *ssa1*Δ, and *hsp82*Δ) in the logarithmic phase. Sti1 exhibited a whole-cell distribution (excluding vacuoles) in all strains. Scale bar: 5 μm. (B) The subcellular distribution of GFP-Sti1 at 48 h of stationary phase. WT cells showed distinct dual-focus aggregates, while *ssa1*Δ and *hsp82*Δ mutants formed intense perinuclear aggregates enveloping the nucleus. Scale bar: 5 μm. (C) Percentage of yeast cells with cytoplasmic and perinuclear Sti1 aggregates in gene knockout strains (*ssa1*Δ, *hsp82*Δ, *hsp104*Δ, and *hsp42*Δ) at 48 h of stationary phase, and correlation analysis relative to WT. In gene knockout strains, Sti1 retained dual-focus localization in 1.35% ± 0.52%, 1.43% ± 0.25%, 1.64% ± 0.73% and 2.38% ± 0.30% of cells at 48 h, respectively (mean ± SD). (D) The subcellular distribution of GFP-Sti1 at 72 h of stationary phase. WT cells maintained clear dual-focus aggregates, whereas *ssa1*Δ and *hsp82*Δ mutants exhibited only diffuse perinuclear accumulation. Scale bar: 5 μm. (E) Percentage of yeast cells with cytoplasmic and perinuclear Sti1 aggregates in gene knockout strains (*ssa1*Δ, *hsp82*Δ, *hsp104*Δ, and *hsp42*Δ) at 72 h of stationary phase, and correlation analysis relative to WT. In gene knockout strains, Sti1 retained a dual-focus localization in 2.76% ± 1.06%, 2.57% ± 0.44%, 2.19% ± 0.69% and 2.11% ± 1.08% of cells at 72 h, respectively (mean ± SD). (F) The subcellular distribution of GFP-Sti1 under rapid glucose deprivation. Punctate aggregation was significantly reduced in *ssa1*Δ and *hsp82*Δ mutants. Scale bar: 5 μm. (G) Percentage of yeast cells with cytoplasmic and perinuclear Sti1 aggregates in gene knockout strains (*ssa1*Δ, *hsp82*Δ, *hsp104*Δ, and *hsp42*Δ) during rapid glucose deprivation, and correlation analysis relative to WT. In gene knockout strains, Sti1 retained dual-focus localization in 8.88% ± 0.16%, 8.47% ± 0.16%, 7.97% ± 0.89%, and 9.61% ± 0.50% of cells, respectively (mean ± SD). Error bars represent the SD of the mean (n = 3) for each assay. For each independent replicate, at least 100 cells were quantified. Statistical analysis was performed using a two-tailed unpaired t test (***P < 0.001 and ****P < 0.0001).

alignment between human STIP1 and yeast Sti1, identifying evolutionarily conserved interaction sites: K9 (yeast)/K8 (human) and K266 (yeast)/K228 (human) (Figure 6A). To dissect the residue-specific regulatory mechanisms, we generated Myc-tagged Sti1 mutants (K9A, K266A, and K9A K266A) in GFP-Ssa1 and GFP-Hsp82 backgrounds. Microscopic analysis revealed that: (1) in the GFP-Ssa1 background, all mutants exhibited uniform nucleocytoplasmic distribution (excluding vacuoles) during the logarithmic phase (Supplementary Figure S7A), formed perinuclear aggregates at 48 h, and developed cytoplasmic foci at 72 h (Supplementary Figure S7B,C,G), showing no significant difference from WT; (2) in the GFP-Hsp82 background, all mutants displayed whole cell distribution (excluding vacuoles) during logarithmic growth (Supplementary Figure S7D) and formed nuclear aggregates at 48 h (Supplementary Figure S7E,F,H), again indistinguishable from WT. Thus, Sti1 mutations in K9/K266 residue(s) did not alter the localization of Ssa1 or Hsp82 across growth phases.

To elucidate the functional significance of the conserved lysine residues, we generated site-specific mutants (K9A, K266A, and K9A K266A) in the GFP-Sti1 strain and performed subcellular localization analysis in GMM. While all mutants exhibited whole cell distribution (excluding vacuoles) during the logarithmic phase (Figure 6B), their dynamic localization under the stationary phase and rapid glucose deprivation revealed functional divergence: (1) the K9A and K9A K266A mutants completely lost the ability to form cytoplasmic aggregates upon glucose deprivation and only produced perinuclear aggregates in the stationary phase (Figure 6C,E,G); and (2) in contrast, the K266A mutant formed both cytoplasmic and perinuclear aggregates, resembling the WT pattern (Figure 6C,E,G). Specifically, at 48 h of stationary phase, the two K9-related Sti1 mutants (K9A and K9A K266A) retained dual-focus localization in 1.51% ± 0.63% and 1.28% ± 0.31% of cells, respectively (mean ± SD) (Figure 6D). At 72 h of stationary phase, the corresponding values were 8.35% ± 0.15% and 8.38% ± 0.25% (mean ± SD) (Figure 6F). Under rapid glucose deprivation, mutant Sti1 exhibited dual-focus localization in 10.44% ± 0.93% (K9A) and 10.17% ± 0.65% (K9A K266A) of cells (mean ± SD) (Figure 6H). Thus, these data demonstrated that K9 is a deterministic residue regulating the formation of Sti1 cytoplasmic aggregates.

To investigate the mechanism by which the K9 residue regulates the formation of Sti1 cytoplasmic aggregates, we conducted Co-IP assays under native conditions. Quantitative analysis revealed the following: (1) Sti1 exhibited weak transient binding with Ssa1 in all strains (K9A and K9A K266A) (Supplementary Figure S8A,B), suggesting that K9 modulated Ssa1-Sti1 co-condensation via structural variation or long-range electrostatic steering; and (2) Sti1 exhibited robust interaction with Hsp82, while the K266A mutation reduced such binding (Supplementary Figure S8C,D). These findings indicated that the K9 residue of Sti1 did not contribute to the formation of intracellular Ssa1 condensates; it was likely to regulate the chaperone microenvironment through an alternative mechanism. Although previous studies have established the functional relevance of these residues in chaperone interactions, site-specific mutations might also alter protein conformation and/or post-translational modification status. To dissect the structural and potential regulatory roles of K9, we purified recombinant Sti1(K9A) from *E. coli* BL21(DE3) using Ni-NTA affinity chromatography. *In vitro* reconstitution assays under varying ionic strengths (0–100 mM NaCl in 25 mM Tris-HCl, pH 7.5) revealed that the Sti1(K9A) mutant exhibited a reduced capacity for phase separation (Supplementary Figure S8E). The structural mechanisms underlying this phenomenon require further investigation. In parallel, to elucidate the specific post-translational modification status of K9, we first predicted potential modifications at this residue through dbPTM (Database of Protein Post-Translational Modifications), which indicated the possibility of succinylation (Supplementary Figure S8F). Therefore, we performed immunoprecipitation assays using a succinylation-specific antibody to examine changes in modification of the Myc-Sti1 fusion protein before and after mutation at the cellular level. However, due to the inherently low succinylation level of Sti1, mutation at the K9 residue did not yield a clearly discernible difference in modification (Supplementary Figure S8G). Qualitative analysis via antibody detection was not feasible owing to interference from the fusion tag and limitations in purification conditions *in vitro* (Supplementary Figure S8H). It seemed that the Sti1 K9 residue would not be succinylated, and at least succinylation was not related to Sti1 cytoplasmic aggregation, if it was.

Potential biological functions of Sti1

Previous studies have demonstrated that Sti1 participates in the cellular response to carbon source stress and maintains mitochondrial morphological integrity [41]. We therefore hypothesized that Sti1, especially its LLPS, function is closely linked to carbon metabolism. To test this hypothesis, we examined the growth curves of five yeast strains—WT, K9A, K266A, *sti1*Δ, and *ssa1*Δ—in glucose medium. The results revealed that all mutant strains exhibited growth similar to the WT strain across all phases (logarithmic, diauxic shift, and stationary), with no significant differences (Figure 7A). This indicated that gene deletion or point mutations did not affect yeast growth in glucose-rich medium. Furthermore, impairment of protein degradation regulated by the PQC system due to gene knockout or mutation might lead to a reduced intracellular protein pool in stationary-phase cells, potentially affecting response rates. To assess the protein pool and relative proteostasis in stationary-phase cells of different strains, we performed growth recovery assays. Compared to WT, the *sti1*Δ and *ssa1*Δ strains exhibited significantly lower recovery rates upon re-entry into the logarithmic and diauxic shift phases, while the K9A strain displayed an intermediate phenotype (Figure 7B and Supplementary Table S4). Thus, Sti1 and Ssa1 regulated the protein pool in stationary-phase cells, ensuring rapid resumption of growth after nutrient recovery.

What functional proteins are closely associated with Sti1-containing aggregates under different nutritional states, and what key biological functions do they perform? To address this, we affinity-purified Sti1 from cultures at different growth phases and under carbon starvation, and analyzed its interacting proteins to elucidate Sti1's potential functions. We also performed nucleocytoplasmic fractionation on stationary-phase cells to analyze functional differences between aggregates in these two compartments (Supplementary Figure S9A,B). GO enrichment analysis of the 1050 proteins interacting with Sti1 in log-phase cells revealed their involvement in crucial biological processes, such as ribosome biogenesis and functional protein translation (Supplementary Figure S9C), suggesting that Sti1 potentially regulated protein synthesis to sustain normal cellular activities during rapid growth. GO analysis of the 977 Sti1-interacting proteins from stationary-phase cells showed enrichment for processes including ribonucleo-

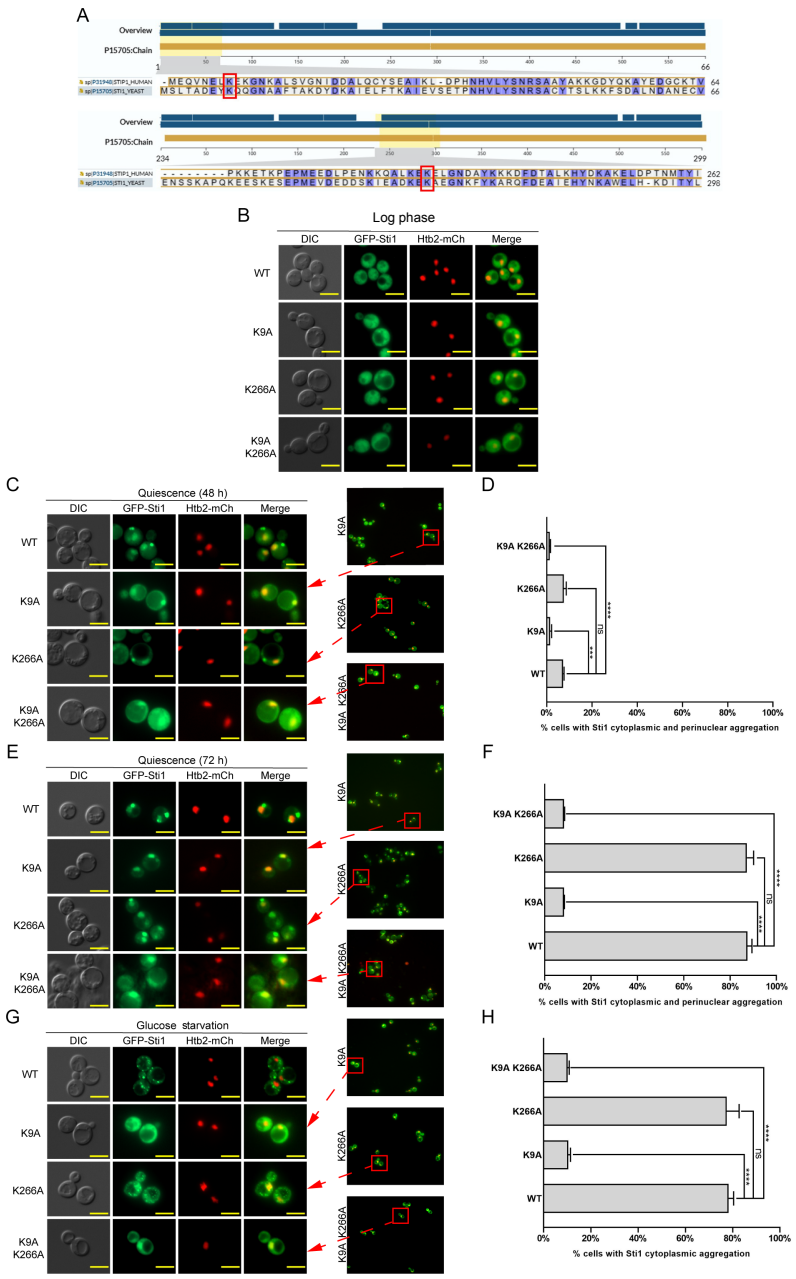


Figure 6. Sti1 K9 is a critical residue regulating its involvement in aggregate formation and its capacity for phase separation (A) Evolutionary conservation analysis of Hsp70/Hsp90-binding lysine residues. Sequence alignment demonstrated conserved spatial positioning of critical lysine residues (human K8/K228 corresponding to yeast K9/K266) at the co-chaperone interaction interface. (B) The subcellular distribution of GFP-Sti1 in various strains (WT, K9A, K266A, and K9A K266A double mutant) in the logarithmic phase. Sti1 exhibited a whole-cell distribution (excluding vacuoles) in all strains. Scale bar: 5 μm. (C) The subcellular distribution of GFP-Sti1 at 48 h of stationary phase. The WT and K266A strains began to form distinct dual-focus aggregates, while the K9A and K9A K266A mutants formed only perinuclear aggregates. Scale bar: 5 μm. (D) Percentage of yeast cells with cytoplasmic and perinuclear Sti1 aggregates in three mutants (K9A, K266A, and K9A K266A) at 48 h of stationary phase, and correlation analysis relative to WT. Sti1 in these mutants retained a dual-punctate localization in 1.51% ± 0.63%, 7.53% ± 1.06%, and 1.28% ± 0.31% of cells, respectively (mean ± SD). (E) The subcellular distribution of GFP-Sti1 at 72 h of stationary phase. The WT and K266A strains maintained clear dual-focus aggregates, whereas the K9A and K9A K266A mutants exhibited only perinuclear aggregation. Scale bar: 5 μm. (F) Percentage of yeast cells with cytoplasmic and perinuclear Sti1 aggregates in three mutants (K9A, K266A, and K9A K266A) at 72 h of stationary phase, and correlation analysis relative to WT. Sti1 in these mutants retained a dual-punctate localization in 8.35% ± 0.15%, 87.29% ± 2.89%, and 8.38% ± 0.25% of cells, respectively (mean ± SD). (G) The subcellular distribution of GFP-Sti1 under rapid glucose deprivation. Punctate aggregate formation was abolished in K9A and K9A K266A mutants. Scale bar: 5 μm. (H) Percentage of yeast cells with cytoplasmic and perinuclear Sti1 aggregates in three mutants (K9A, K266A, and K9A K266A) during rapid glucose deprivation, and correlation analysis relative to WT. Sti1 in these mutants retained a dual-punctate localization in 10.44% ± 0.93%, 77.52% ± 5.22%, and 10.17% ± 0.65% of cells, respectively (mean ± SD). Error bars represent the SD of the mean (n = 3) for each assay. For each independent replicate, at least 100 cells were quantified. Statistical analysis was performed using a two-tailed unpaired t test (ns, not significant; ***P < 0.001 and ****P < 0.0001).

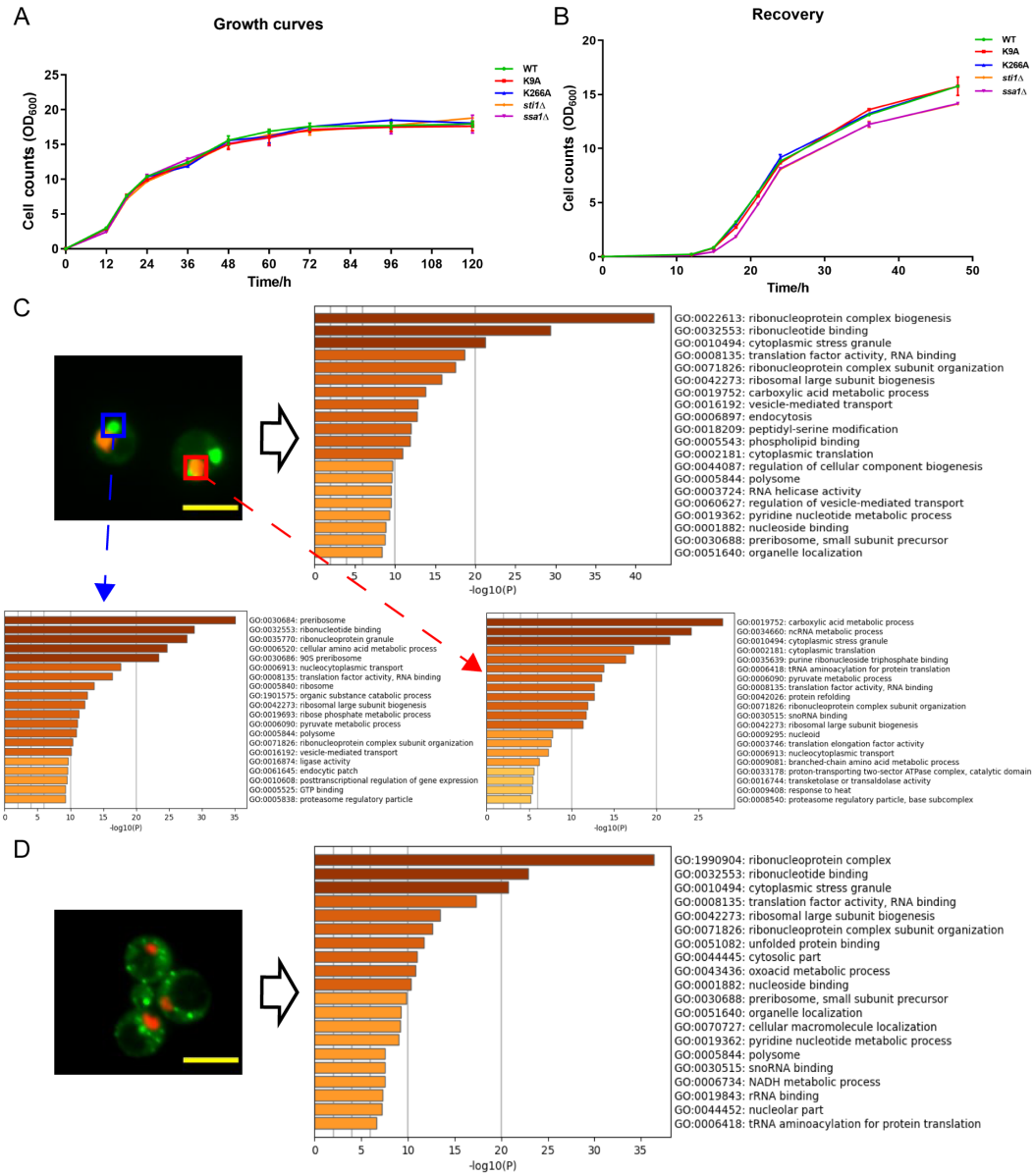


Figure 7. Potential biological functions of Sti1 (A) Growth curves of the five strains (WT, K9A, K266A, *sti1*Δ, and *ssa1*Δ) in glucose medium over 120 h. All strains exhibited similar growth patterns with no significant differences (data not shown). Error bars represent standard deviation. (B) Growth recovery curves of the five strains in glucose medium. The *sti1*Δ and *ssa1*Δ strains showed clear deviations from WT upon entry into the logarithmic and diauxic shift phases. The K9A strain displayed an intermediate phenotype. Error bars indicate the SD of the mean ($n = 3$) for each assay; correlation analysis is provided in Supplementary Table S4. (C) Biological processes associated with Sti1 during the stationary phase. GO enrichment analysis was performed using Metascape on 977 Sti1-interacting proteins from stationary-phase cultures, highlighting the top 20 enriched biological processes. These include ribonucleoprotein complex biogenesis, ribonucleotide binding, cytoplasmic stress granules, translation factor activity, ribonucleoprotein complex subunit organization, ribosomal large subunit biogenesis, carboxylic acid metabolic process, vesicle-mediated transport, endocytosis, peptidyl-serine modification, phospholipid binding, cytoplasmic translation, regulation of cellular component biogenesis, polysome, RNA helicase activity, regulation of vesicle-mediated transport, pyridine nucleotide metabolic process, nucleoside binding, preribosome, and organelle localization. Further analysis of Sti1 interactors enriched in the cytoplasmic fraction after nucleo-cytoplasmic separation revealed associations with preribosome, cellular amino acid metabolism, nucleocytoplasmic transport, translation factor activity, organic substance catabolic process, ribose phosphate metabolic process, pyruvate metabolic process, vesicle-mediated transport, and ligase activity. Sti1 interactors enriched in the perinuclear region were primarily linked to carboxylic acid metabolic process, cytoplasmic stress granules, cytoplasmic translation, pyruvate metabolic process, protein refolding, nucleocytoplasmic transport, and heat shock proteins. (D) Biological processes associated with Sti1 under rapid glucose deprivation. GO enrichment analysis using Metascape was performed on 992 Sti1-interacting proteins from cultures subjected to rapid glucose deprivation, showing the top 20 enriched biological processes. These include ribonucleoprotein complex, ribonucleotide binding, cytoplasmic stress granules, translation factor activity, RNA binding, ribosomal large subunit biogenesis, ribonucleoprotein complex subunit organization, unfolded protein binding, oxoacid metabolic process, nucleoside binding, preribosome, organelle localization, cellular macromolecule localization, pyridine nucleotide metabolic process, polysome, snoRNA binding, NADH metabolic process, rRNA binding, nucleolar part, and tRNA aminoacylation for protein translation.

protein synthesis, stress granule formation, vesicle-mediated transport, and protein translation (Figure 7C). This indicated that in the stationary phase, in addition to modulating translation, Sti1 contributed to proteostasis via vesicle transport and endocytosis. Furthermore, its role in mediating stress granule formation aligned with our prior localization data (Figure 1C). Subsequent fractionation of stationary-phase cells allowed separate GO analysis of Sti1 interactors in the cytoplasm and nucleus. Cytoplasmic interactors were associated with diverse metabolic processes, including ribosome biogenesis, nucleocytoplasmic transport, and vesicle transport (Figure 7C), suggesting that cytoplasmic Sti1 aggregates likely participate in degrading misfolded proteins and regulating protein synthesis during quiescence. Nuclear interactors were linked to processes such as stress granules, translation, nucleocytoplasmic transport, and heat shock proteins (Figure 7C), implying an intrinsic connection between Sti1 and nuclear accumulation chaperones, such as Hsp104 and Hsp82, in regulating nucleocytoplasmic proteostasis (Figure 7C). GO enrichment analysis of the 992 proteins interacting with Sti1 under rapid glucose deprivation revealed their involvement in diverse biological processes, including ribonucleoprotein complexes, ribonucleotide binding, cytoplasmic stress granules, and preribosomes (Figure 7D).

We next analyzed changes in the Sti1 interactome between the logarithmic and stationary phases. We identified 729 common interacting proteins shared between both phases (Supplementary Figure S9D), primarily involved in processes such as preribosome, ribosomal large subunit biogenesis, cytoplasmic stress granules, and organic acid metabolism (Supplementary Figure S9D). This suggested that as cells transition from rapid growth to quiescence, these key proteins involved in ribosome biology, stress response, and metabolism maintain a stable association with Sti1, aiding cellular adaptation to a gradually nutrient-depleted environment. Comparing phase-specific interactions, we found 682 proteins that interacted more strongly with Sti1 during the logarithmic phase. These were enriched for ribosome biogenesis, chaperone complexes, preribosomes, organic acid biosynthetic processes, translation factor activity, and the Ccr4-Not core complex (Supplementary Figure S9D). This finding implied that as yeast cells gradually entered the stationary phase, they downregulated *de novo* ribosome generation and partially abandoned translation/transcription processes, enabling a low-energy dormant state for prolonged survival. Conversely, 535 proteins exhibited stronger interactions with Sti1 during the stationary phase, showing enrichment for endocytosis, ribonucleoprotein complex biogenesis, protein refolding, clathrin-coated vesicles, and regulation of cellular component organization (Supplementary Figure S9D). This indicated that, compared to the log phase, Sti1 in the stationary phase was more engaged in protein degradation pathways to maintain proteostasis. Furthermore, our mass spectrometry data also identified numerous chaperones and PQC components (Supplementary Table S5), which further confirmed the physical interactions among them in addition to the aforementioned co-localization evidence.

The role of the chaperone system in nutrient signal-mediated protein aggregate formation

Ssa1, Hsp82, and the PQC-related chaperones regulated Sti1 condensate formation. To better understand the function of Sti1 under carbon source starvation, we examined the subcellular distribution of Ssa1, Hsp82, Hsp104, and Hsp42 in a *sti1*Δ background. Notably, under both stationary phase and glucose deprivation conditions, the cytoplasmic aggregation of Ssa1, Hsp104, and Hsp42 was abolished (Figure 8 and Supplementary Figure S10), with only perinuclear aggregates remaining. Specifically, in the *sti1*Δ strain during the stationary phase, Ssa1, Hsp104, and Hsp42 maintained a WT localization pattern in 3.28 ± 0.96%, 3.74 ± 0.71%, and 3.16 ± 0.79% of cells, respectively (mean ± SD) (Figure 8 and Supplementary Figure S10D,E). Under rapid glucose deprivation, Hsp104 and Hsp42 retained WT localization in 7.11% ± 0.41% and 6.85% ± 1.07% of cells, respectively (mean ± SD) (Supplementary Figure S10D,E). This perinuclear localization pattern closely resembled that of Sti1 in *ssa1*Δ or *hsp82*Δ cells. Furthermore, based on Sti1's co-chaperone function and its relationship to Ssa1 and Hsp82, we examined the distribution of Hsp82 and Ssa1 in the *ssa1*Δ and *hsp82*Δ backgrounds, respectively, to clarify the functional hierarchy among these three proteins. We observed that the localization of Hsp82 remained unaffected, while Ssa1 was restricted to perinuclear aggregation (Figure 8)—a pattern resembling that of Sti1—indicating that Ssa1 aggregation is dependent on Sti1, whereas Hsp82 operates independently within this regulatory network. Therefore, Sti1 plays an important role in the phase separation of Ssa1, thereby establishing the foundation for cytoplasmic condensate formation (Figure 9).

Discussion

S. cerevisiae is a widely used model for many biological processes, including nutrient sensing and responding and the maintenance of proteostasis. Here, we uncovered a coordination between nutrient starvation and protein aggregation. Cytoplasmic misfolded proteins were sequestered into the PQC inclusions, and many chaperones participated in these compartments. In the stationary phase, when nutrients are depleted, the PQC machinery, represented by Hsp104 and Hsp42, participates in regulating the formation of intracellular protein aggregates (Figure 1). As a central marker for both perinuclear JUNQ and cytoplasmic IPOD compartments, Hsp104 exhibited dual-focus localization under nutritional stress, confirming two distinct types of protein aggregates in stationary-phase yeast cells (Figure 1). Unexpectedly, the co-chaperone Sti1 showed co-localization with nearly all marker proteins under nutrient deprivation, with complete overlap observed, particularly with Hsp104 and Ssa1 (Figures 1 and 2). This suggested that Sti1 probably played a role in cytoplasmic protein aggregates during carbon source limitation. Sti1 puncta also partially co-localized with SGs (Figures 2 and 7, and Supplementary Figure S9), indicating that Sti1 was likely involved in some stress responses, in addition to PQC protein aggregation and CytoQ (marked by Hsp42) partly.

Building on the diverse properties of PQC components, we further investigated the biophysical properties of Sti1 aggregates. Unexpectedly, we found that Sti1 and Ssa1 formed cytoplasmic aggregates via LLPS, while perinuclear structures exhibited significantly reduced fluidity (Figure 4 and Supplementary Figure S3). According to previous reports and the widely used PQC marker localization, cytosolic protein aggregates are classified as IPODs, which are dense and insoluble, whereas perinuclear aggregates correspond to the dynamic, soluble JUNQ. This established dichotomy stands in contrast to the biophysical properties we observed for Sti1 aggregates in these two subcellular locations. First, we posited that the IPOD inclusions contained densely packed, amyloid-like aggregates of misfolded proteins, while

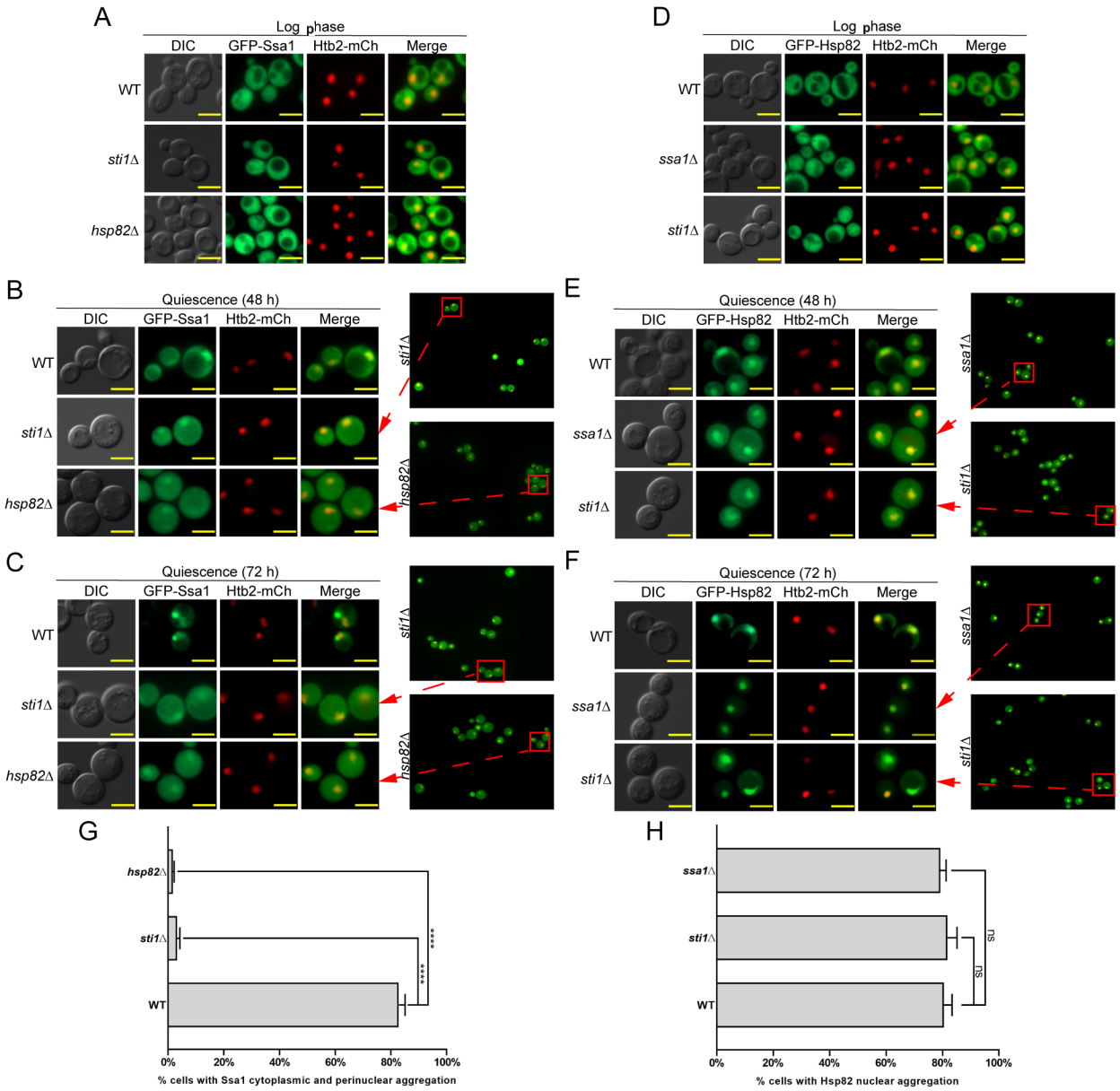


Figure 8. The role of the chaperone system in nutrient signal-mediated protein aggregate formation (A–C) The subcellular distribution of GFP-Ssa1 in various strains (WT, *sti1*Δ, and *hsp82*Δ) across growth phases. In the knockout strains, Ssa1 no longer formed cytoplasmic aggregates in the stationary phase and exhibited only perinuclear aggregation. Scale bar: 5 μm. (D–F) The subcellular distribution of GFP-Hsp82 in various strains (WT, *ssa1*Δ, and *sti1*Δ) across growth phases. The localization of Hsp82 remained unaffected in knockout strains, showing uniform nucleocytoplasmic distribution (vacuoles excluded) in the logarithmic phase and nuclear aggregation in the stationary phase. Scale bar: 5 μm. (G) Percentage of yeast cells with cytoplasmic and perinuclear Ssa1 aggregates in gene knockout strains (*sti1*Δ and *hsp82*Δ) during the stationary phase, and correlation analysis relative to WT. In gene knockout strains, Ssa1 retained a dual-focus localization in 3.28% ± 0.96% and 1.74% ± 0.44% of cells, respectively (mean ± SD). (H) Percentage of yeast cells with nuclear Hsp82 aggregates in gene knockout strains (*sti1*Δ and *ssa1*Δ) during the stationary phase, and correlation analysis relative to WT. Nuclear Hsp82 aggregates were observed in 81.77% ± 3.38% and 79.21% ± 2.07% of cells, respectively (mean ± SD). Error bars represent the SD of the mean ($n = 3$) for each assay. For each independent replicate, at least 100 cells were quantified. Statistical analysis was performed using a two-tailed unpaired *t* test (ns, not significant. ****$P < 0.0001$).

chaperones were distributed on the surface of these aggregates in a dynamic and soluble state, consistent with LLPS. This architecture could serve a dual function: effectively shielding the internal misfolded proteins while allowing for rapid dissolution of the aggregate under appropriate conditions, facilitating subsequent refolding or autophagic clearance. Second, although the perinuclear Sti1 aggregates we observed differ markedly in morphology and biophysical properties from the reported JUNQ (typically described under heat shock), we did not detect a canonical, concentrated JUNQ structure adjacent to the nucleus under our nutritional stress conditions. However, these perinuclear Sti1 aggregates were found to contain classic JUNQ marker proteins, such as Cdc48 and Rpn1 (data not shown), as evidenced by fluorescence co-localization and mass spectrometry. We therefore speculated that perinuclear Sti1

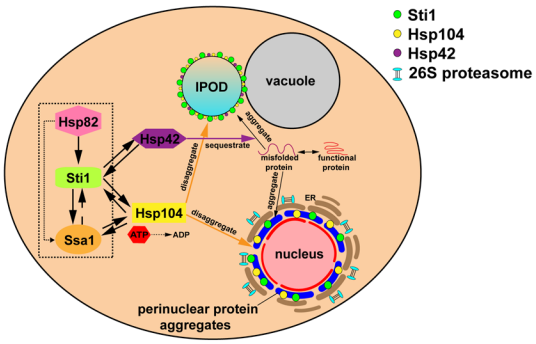


Figure 9. Nutrient-dependent formation of Sti1-mediated and PQC-related protein aggregates Co-localization analyses revealed robust spatial coordination between Sti1 condensates and the chaperone system, establishing their coupled mechanistic roles in chaperone-mediated protein disaggregation and quality control compartmentalization. Under nutrient deprivation, Sti1 likely regulates the biogenesis of cytoplasmic condensates via its phase-separating activity, synergizing with Hsp104, Hsp42 and Ssa1 chaperone triad to drive perinuclear protein aggregate assembly. This process was further amplified through functional crosstalk with Cdc48 (a p97/VCP ortholog). Notably, cytosolic aggregation of Sti1 itself exhibited a strict dependence on the cooperative actions of Hsp104 (disaggregase), Hsp42 (aggregase), and Ssa1 (Hsp70 ATPase). Furthermore, Sti1 served as a critical adaptor for Hsp42-mediated condensates to the IPOD compartment. The potentially viable dynamic equilibrium model: During early quiescence (48 h), Sti1 preferentially nucleates perinuclear condensates co-localizing with JUNQ markers, facilitating proteasomal clearance of misfolded proteins. At later stages, Ssa1/Hsp82-guided LLPS drives cytoplasmic condensate formation, sequestering IPOD while establishing stress-resistant compartments for functional protein preservation.

aggregates might represent a nutritionally stress-specific variant of JUNQ or a related structure. The defining features and specific protein components of this putative stress-specific perinuclear compartment warrant further investigation. Furthermore, under rapid glucose deprivation, most chaperones, including Sti1, formed puncta. However, Sti1 showed only partial co-localization with other aggregates, such as CytoQ (marked by Hsp42) or stress granules (marked by Pab1). This suggested that Sti1 was functionally heterogeneous during nutritional stress, potentially participating in diverse intracellular structures and biological processes. Compared to its dichotomous localization in quiescent cells (IPOD and perinuclear aggregate), Sti1 might assume a broader functional repertoire under these stress conditions, although the precise details require further elucidation. On a technical note, because the mCherry fluorescent signal was substantially weaker than that of GFP, the reliability of co-localization observations based solely on fluorescence was uncertain (Figure 1). To address this, we performed Sti1 pull-down assays followed by mass spectrometry. The confirmed presence of the aforementioned proteins in the mass spectrometry results not only validated the co-localization data but also reinforced the notion of Sti1's functional pleiotropy (Figure 7).

Given the critical role of Sti1 and Ssa1 phase separation in PQC compartment formation, we dissected the underlying molecular mechanism governing their phase separation. Although Ssa1 and Sti1 co-localize in stationary-phase cells, they showed different abilities in condensation *in vitro* (Figure 4 and Supplementary Figure S3), indicating that Ssa1 and Sti1 played diverse roles in PQC aggregation. Some reports support that IDR is important for LLPS [28,52], and there are 3 IDRs in Sti1 (Supplementary Figure S5). Subsequent deletion experiments proved that any of the 3 IDRs was necessary for Sti1 LLPS (Supplementary Figure S5). Given that Sti1 phase separation depends on Hsp82 and Ssa1, we hypothesized that this regulation might be mediated by their direct interaction (Figure 5). Informed by findings in animal cells, which identified lysine residues K8 and K228 as essential for this interaction, we performed sequence alignment. This analysis revealed that these two lysines were conserved in yeast. We therefore constructed K9A and K226A mutant strains (corresponding to K8 and K228, respectively). Our investigation using these mutants identified K9 as a critical residue governing the formation of cytosolic Sti1 condensates (Figure 6). Then, we wanted to know how K9 regulates condensate assembly. Bioinformatics tool prediction suggested K9 as a potential site for succinylation. However, employing a succinylation-specific antibody, we did not detect a significant difference in succinylation levels between WT and K9A mutant proteins (Supplementary Figure S8). Elucidating the post-translational modification landscape at this specific residue will be a focus of our subsequent work.

Recent research has demonstrated that ribosome-binding proteins (RBPs) undergo LLPS during translational arrest to protect nascent peptide chains and mRNAs [53–56]. Similarly, Sti1-mediated LLPS might constitute a protective pausing mechanism that preserves macromolecular integrity during nutrient stress and permits rapid recovery once nutrients become available again. Furthermore, integrating our findings with prior studies on Sti1/Hop, the current data indicated that Sti1 was predominantly cytoplasmic. However, heat shock treatment of 293T cells or hydroxyurea treatment of murine cells induces cell cycle arrest, leading to pronounced nuclear accumulation of Sti1/Hop [38,39]. Notably, under stress conditions in HeLa cells, Hop is observed to form protein aggregates [45]. A comparative localization analysis revealed that the patterns induced by carbon source depletion were distinct from those described above. We therefore performed preliminary stress tests (temperature, pH) on various yeast strains. The results showed that yeast cells formed low-abundance punctate aggregates specifically under heat shock, which were structurally distinct from aggregates induced by carbon source depletion (Supplementary Figure S11A). Interestingly, deletion of *SSA1* increased the number of intracellular puncta, a phenomenon likely linked to the biological function of Sti1 as a cochaperone (Supplementary Figure S11A). Moreover, the aggregates formed under the two distinct conditions—the stationary phase and rapid glucose deprivation—exhibit morphological differences. First, the environmental contexts and formation timelines differ substantially: the stationary phase is characterized by depletion of fermentable carbon sources but the presence of metabolically generated ethanol and other byproducts, whereas rapid glucose deprivation involves solely the absence of glucose. Second, the cell state (logarithmic vs stationary phase) inherently influences aggregate morphology. To compare these two aggregate types, we performed a comparative proteomic analysis. Although the aggregation processes differ, the interacting proteins and associated biological functions were largely consistent between the two states. While some distinct interacting proteins were identified in each stress condition, their abundance values were notably low (Supplementary Figure S11). Thus, we demonstrated that regardless of the kinetics of the stress response, Sti1 recruited a conserved set of proteins related to ribosomes, translation, and stress granules

to protect cells under pressure (Supplementary Figure S11). Crucially, irrespective of the aggregation mechanism, both patterns—compared to the uniform nucleocytoplasmic distribution of Sti1 under non-stress conditions—represent specific cellular manifestations of carbon source starvation stress.

Hsp70, Hsp90 and their co-chaperones play important roles in proteostasis maintenance. We found that Ssa1 and Sti1 also joined PQC compartments in addition to the well-known Hsp42 and Hsp104. Deletion of *STI1* abolished Hsp42, Hsp104 and Ssa1 IPOD localization. We therefore proposed a functional interaction network integrating Sti1 with other chaperones (Ssa1, Hsp82, Hsp104, and Hsp42) based on experimental evidence [28]. To better understand the relationship among Hsp82, Ssa1 and Sti1, we performed single-gene knockouts. Deletion of *SSA1* or *HSP82* significantly suppressed Sti1 cytoplasmic condensate formation, and in *sti1*Δ or *hsp82*Δ mutants, the localization of Ssa1 was consistently disrupted (Figure 8). These subcellular localization data indicated that although Hsp82 interacted with Sti1 and Ssa1 only in the exponential phase, Hsp82 served as a regulator of Sti1 condensate formation, and there was mutual regulation between Sti1 and Ssa1 under nutrient stress conditions (Figure 9). Hsp90 can modulate LLPS by targeting intrinsically disordered regions in client proteins [57]. Thus, deletion of *HSP82* disrupted this balance, leading to aberrant accumulation of Sti1/Ssa1 at ribosomal sites. In light of this, we proposed that Sti1 was far more than a static linker but rather a highly dynamic protein. It might function as a scaffolding and recruitment platform, integrating the substrate recognition and processing functions of Ssa1 (Hsp70), whereas Hsp82 (Hsp90) likely acts at a more upstream or parallel regulatory node, indirectly modulating the stability or composition of aggregates through its conformational cycle and maturation of specific client proteins [22]. Consequently, in the stationary phase or glucose deprivation, cytoplasmic Sti1 in *hsp82*Δ failed to form functional aggregates, which might explain why the K266A mutant retained the ability to form stable cytoplasmic condensates (Figure 6). Alternatively, there is another possibility that Hsp82 indirectly regulates the localization of Ssa1 or Sti1 by modulating the other, although the underlying mechanism remains to be further explored. Furthermore, Hsp82 may function by correctly folding a "third-party" factor that is essential for Sti1 phase separation; Hsp82 itself could act as a "modulator" of liquid-liquid phase separation, with its ATPase cycle influencing the local microenvironment [58]; although weak direct interactions may exist, its primary role is likely one of conformational regulation [59]. Based on recent evidence demonstrating that Sti1 can independently form cytoplasmic aggregates to sequester misfolded proteins and maintain proteostasis—a function that does not rely on the ATPase activity of Hsp90—we considered it plausible that Hsp82 exerted its influence primarily through indirect or weak interactions, likely mediated by conformational regulation [44]. The subcellular localization analysis indicated that Sti1 was more sensitive to glucose availability than Ssa1 (Figure 3 and Supplementary Figure S2), suggesting that Sti1 played a more fundamental role in nutrient stress-induced protein aggregation. In the canonical chaperone cascade, nascent polypeptides first undergo Hsp70-mediated conformational remodeling, followed by transfer to Hsp90—assisted by the adaptor Sti1/Hop—for final maturation. Therefore, knockout experiments demonstrated that loss of Ssa1 impaired this nascent-chain folding cascade, thereby compromising Sti1′s function in maintaining proteostasis—a dependency reflected in the phenotype of the *sti1*Δ mutant. Notably, the K9-site mutation disrupted the formation of cytoplasmic Sti1 condensates through structural and posttranslational mechanisms, independent of its canonical chaperonerelated biological functions (Supplementary Figures S7 and S8).

Furthermore, subsequent gene knockout results confirmed that Sti1 also contributed to PQC functionality (Figure 8 and Supplementary Figure S10), and conversely, proper PQC activity regulated Sti1 aggregation (Supplementary Figure S6). Based on these interactions, we proposed that Sti1 aggregation was mechanistically linked to the biological functions of Hsp104, Hsp42 and Ssa1. Under nutrient deprivation, Sti1 likely employs its intrinsic phase separation capacity to promote the formation of condensates in the cytoplasm in conjunction with Hsp104, Hsp42 and Ssa1, thereby facilitating perinuclear protein aggregate assembly and cooperating with Cdc48 (Figure 9) [6–8,29]. Concurrently, Hsp104, Hsp42, and Ssa1 were indispensable for Sti1 cytoplasmic condensate formation (Figure 9). Additionally, Sti1 might regulate Hsp42-mediated condensates to IPOD compartments (Figure 9). Within this framework, we proposed a dynamic homeostasis model: during early culture stages (48 h), Sti1 preferentially forms perinuclear aggregates associated with JUNQ and proteasomal complexes to clear misfolded proteins. As cultures progress, LLPS-driven cytoplasmic aggregates emerge, providing protective microenvironments for functional proteins during stress adaptation (Figure 9). Crucially, these aggregates exhibited glucose-responsive dynamics—a hallmark of biologically regulated phase separation systems (Figure 7). The proposed dynamic model was further corroborated by mass spectrometry-based proteomics, which revealed that Sti1 ubiquitously regulated protein translation and synthesis across different growth phases and, under stationary-phase stress conditions, collaborated with the PQC machinery to maintain proteostasis (Figure 7, Supplementary Figure S9 and Supplementary Table S5).

In summary, this study reveals that: (1) nutrient deprivation induces the formation of functional protein aggregates within cells. From a novel perspective, it also highlights the essential role of the co-chaperone Sti1 in this process and elucidates the mechanisms governing its dynamic localization; (2) Sti1 aggregation at IPOD is LLPS-driven, which is different from that at JUNQ; and (3) Sti1, Ssa1, Hsp82, the well-known Hsp42 and Hsp104 organize a chaperone network to participate in protein quality control and proteostasis maintenance.

Supplementary Data

Supplementary data are available at *Acta Biochimica et Biophysica Sinica* online.

Data Availability

All the original data can be accessed upon reasonable request from the corresponding authors.

Author Contribution

Jiawei Chen: investigation, methodology, validation, visualization, data curation, formal analysis, writing (original draft). Jiayu Zhou: investigation, data curation, visualization. Keren Sun: investigation, visualization. Hanlin Zhang: investigation, visualization. Yanqiu Ji: investigation, methodology. Letong Li: investigation. Wanjie Li: conceptualization, writing—review & editing, visualization, supervision. Fei Dou: conceptualization, writing—review &

editing, visualization, supervision.

Acknowledgements

We thank members of the Dou laboratory for useful discussions. We thank the Experimental Technology Center of the College of Life Science of Beijing Normal University for technical help. We thank Prof. Ying Zhang from Beijing Normal University for her comments and advice.

Funding

This work was supported by the grant from the National Natural Science Foundation of China (No. 32470820).

Conflict of Interest

The authors declare that they have no conflict of interest.

References

1. Balch WE, Morimoto RI, Dillin A, Kelly JW. Adapting proteostasis for disease intervention. *Science* 2008, 319: 916–919
2. Hartl FU, Bracher A, Hayer-Hartl M. Molecular chaperones in protein folding and proteostasis. *Nature* 2011, 475: 324–332
3. Bukau B, Weissman J, Horwich A. Molecular chaperones and protein quality control. *Cell* 2006, 125: 443–451
4. Hartl FU, Hayer-Hartl M. Converging concepts of protein folding *in vitro* and *in vivo*. *Nat Struct Mol Biol* 2009, 16: 574–581
5. Ji CH, Kwon YT. Crosstalk and interplay between the ubiquitin-proteasome system and autophagy. *Mol Cells* 2017, 40: 441–449
6. Kaganovich D, Kopito R, Frydman J. Misfolded proteins partition between two distinct quality control compartments. *Nature* 2008, 454: 1088–1095
7. Kopito RR. Aggresomes, inclusion bodies and protein aggregation. *Trends Cell Biol* 2000, 10: 524–530
8. Rothe S, Prakash A, Tyedmers J. The insoluble protein deposit (IPOD) in yeast. *Front Mol Neurosci* 2018, 11: 237
9. Knowles TPJ, Vendruscolo M, Dobson CM. The amyloid state and its association with protein misfolding diseases. *Nat Rev Mol Cell Biol* 2014, 15: 384–396
10. Reidy M, Kumar S, Anderson DE, Masison DC. Dual roles for yeast Sti1/Hop in regulating the Hsp90 chaperone cycle. *Genetics* 2018, 209: 1139–1154
11. Reidy M, Masison DC. Sti1 regulation of Hsp70 and Hsp90 is critical for curing of *Saccharomyces cerevisiae* [*PSI*+] prions by Hsp104. *Mol Cell Biol* 2010, 30: 3542–3552
12. Nicolet CM, Craig EA. Isolation and characterization of *STI1*, a stress-inducible gene from *Saccharomyces cerevisiae*. *Mol Cell Biol* 1989, 9: 3638–3646
13. Honore B, Leffers H, Madsen P, Rasmussen HH, Vandekerckhove J, Celis JE. Molecular cloning and expression of a transformation-sensitive human protein containing the TPR motif and sharing identity to the stress-inducible yeast protein STI1. *J Biol Chem* 1992, 267: 8485–8491
14. Bhattacharya K, Picard D. The Hsp70-Hsp90 go-between Hop/Stip1/Sti1 is a proteostatic switch and may be a drug target in cancer and neurodegeneration. *Cell Mol Life Sci* 2021, 78: 7257–7273
15. Lee C-, Graf C, Mayer FJ, Richter SM, Mayer MP. Dynamics of the regulation of Hsp90 by the co-chaperone Sti1. *EMBO J* 2012, 31: 1518–1528
16. Lamb JR, Tugendreich S, Hieter P. Tetratrico peptide repeat interactions: to TPR or not to TPR? *Trends Biochem Sci* 1995, 20: 257–259
17. Scheufler C, Brinker A, Bourenkov G, Pegoraro S, Moroder L, Bartunik H, Hartl FU, *et al.* Structure of TPR domain-peptide complexes. *Cell* 2000, 101: 199–210
18. Schmid AB, Lagleder S, Gräwert MA, Röhl A, Hagn F, Wandinger SK, Cox MB, *et al.* The architecture of functional modules in the Hsp90 co-chaperone Sti1/Hop. *EMBO J* 2012, 31: 1506–1517
19. Odunuga OO, Longshaw VM, Blatch GL. Hop: more than an Hsp70/Hsp90 adaptor protein. *Bioessays* 2004, 26: 1058–1068
20. Richter K, Muschler P, Hainzl O, Reinstein J, Buchner J. Sti1 is a non-competitive inhibitor of the Hsp90 ATPase. *J Biol Chem* 2003, 278: 10328–10333
21. Johnson JL, Halas A, Flom G. Nucleotide-dependent interaction of *Saccharomyces cerevisiae* Hsp90 with the cochaperone proteins Sti1, Cpr6, and Sba1. *Mol Cell Biol* 2007, 27: 768–776
22. Roehl A, Wengler D, Madl T, Lagleder S, Tippel F, Herrmann M, Hendrix J, *et al.* Hsp90 regulates the dynamics of its cochaperone Sti1 and the transfer of Hsp70 between modules. *Nat Commun* 2015, 6: 6655
23. Willmund F, del Alamo M, Pechmann S, Chen T, Albanèse V, Dammer EB, Peng J, *et al.* The cotranslational function of ribosome-associated Hsp70 in eukaryotic protein homeostasis. *Cell* 2013, 152: 196–209
24. Shalgi R, Hurt JA, Krykbaeva I, Taipale M, Lindquist S, Burge CB. Widespread regulation of translation by elongation pausing in heat shock. *Mol Cell* 2013, 49: 439–452
25. Kakihara Y, Houry WA. The R2TP complex: discovery and functions. *Biochim Biophys Acta* 2012, 1823: 101–107
26. Schopf FH, Huber EM, Dodt C, Lopez A, Biebl MM, Rutz DA, Mühlhofer M, *et al.* The co-chaperone Cns1 and the recruiter protein Hgh1 link Hsp90 to translation elongation via chaperoning elongation factor 2. *Mol Cell* 2019, 74: 73–87.e8
27. Boulon S, Bertrand E, Pradet-Balade B. HSP90 and the R2TP co-chaperone complex: building multi-protein machineries essential for cell growth and gene expression. *RNA Biol* 2012, 9: 148–154
28. Bhattacharya K, Weidenauer L, Luengo TM, Pieters EC, Echeverría PC, Bernasconi L, Wider D, *et al.* The Hsp70-Hsp90 co-chaperone Hop/Stip1 shifts the proteostatic balance from folding towards degradation. *Nat Commun* 2020, 11: 5975
29. Sathyanarayanan U, Musa M, Bou Dib P, Raimundo N, Milosevic I, Krisko A. ATP hydrolysis by yeast Hsp104 determines protein aggregate dissolution and size *in vivo*. *Nat Commun* 2020, 11: 5226
30. Kikis EA, Gidalevitz T, Morimoto RI. Protein homeostasis in models of aging and age-related conformational disease. *Adv Exp Med Biol* 2010, 694: 138-159
31. Tyedmers J, Mogk A, Bukau B. Cellular strategies for controlling protein aggregation. *Nat Rev Mol Cell Biol* 2010, 11: 777–788
32. Hipp MS, Park SH, Hartl FU. Proteostasis impairment in protein-misfolding and -aggregation diseases. *Trends Cell Biol* 2014, 24: 506–514
33. Boronat S, Cabrera M, Hidalgo E. Spatial sequestration of misfolded proteins as an active chaperone-mediated process during heat stress. *Curr Genet* 2021, 67: 237–243
34. Thirumalaikumar VP, Gorka M, Schulz K, Masclaux-Daubresse C, Sampathkumar A, Skirycz A, Vierstra RD, *et al.* Selective autophagy regulates heat stress memory in *Arabidopsis* by NBR1-mediated targeting of HSP90.1 and ROF1. *Autophagy* 2021, 17: 2184–2199
35. Muller L, Hoppe T. UPS-dependent strategies of protein quality control degradation. *Trends Biochem Sci* 2024, 49: 859–874
36. Wang X, Terpstra EJM. Ubiquitin receptors and protein quality control. *J Mol Cell Cardiol* 2013, 55: 73–84
37. Braunstein I, Zach L, Allan S, Kalies KU, Stanhill A, Tansey WP. Proteasomal degradation of preemptive quality control (pQC) substrates is mediated by an AIRAPL-p97 complex. *Mol Biol Cell* 2015, 26: 3719–3727

38. Daniel S, Bradley G, Longshaw VM, Söti C, Csermely P, Blatch GL. Nuclear translocation of the phosphoprotein Hop (Hsp70/Hsp90 organizing protein) occurs under heat shock, and its proposed nuclear localization signal is involved in Hsp90 binding. *Biochim Biophys Acta* 2008, 1783: 1003–1014
39. Longshaw VM, Dirr HW, Blatch GL, Lässle M. The *in vitro* phosphorylation of the co-chaperone mSTI1 by cell cycle kinases substantiates a predicted casein kinase II-p34cdc2-NLS (CcN) motif. *Biol Chem* 2000, 381: 1133–1138
40. Song HO, Lee W, An K, Lee H, Cho JH, Park ZY, Ahnn J. *C. elegans* STI-1, the homolog of Sti1/Hop, is involved in aging and stress response. *J Mol Biol* 2009, 390: 604–617
41. Hoseini H, Pandey S, Jores T, Schmitt A, Franz-Wachtel M, Macek B, Buchner J, ***et al.*** The cytosolic cochaperone Sti1 is relevant for mitochondrial biogenesis and morphology. *FEBS J* 2016, 283: 3338–3352
42. Gu J, Liu Z, Zhang S, Li Y, Xia W, Wang C, Xiang H, ***et al.*** Hsp40 proteins phase separate to chaperone the assembly and maintenance of membraneless organelles. *Proc Natl Acad Sci USA* 2020, 117: 31123–31133
43. Fang Y, Fliss AE, Rao J, Caplan AJ. *SBA1* encodes a yeast hsp90 cochaperone that is homologous to vertebrate p23 proteins. *Mol Cell Biol* 1998, 18: 3727–3734
44. Rutledge BS, Kim YJ, McDonald DW, Jurado-Coronel JC, Prado MAM, Johnson JL, Choy WY, ***et al.*** Stress-inducible phosphoprotein 1 (Sti1/Stip1/Hop) sequesters misfolded proteins during stress. *FEBS J* 2025, 292: 3634–3658
45. Pare JM, Tahbaz N, López-Orozco J, LaPointe P, Lasko P, Hobman TC, Wickens M. Hsp90 regulates the function of argonaute 2 and its recruitment to stress granules and P-bodies. *Mol Biol Cell* 2009, 20: 3273–3284
46. Shang X, Cao G, Gao H, Li M, Peng G, Ji Y, Zhang Y, ***et al.*** A single site phosphorylation on Hsp82 ensures cell survival during starvation in *Saccharomyces cerevisiae*. *J Mol Biol* 2020, 432: 5809–5824
47. Schiestl RH, Dominska M, Petes TD. Transformation of *Saccharomyces cerevisiae* with nonhomologous DNA: illegitimate integration of transforming DNA into yeast chromosomes and *in vivo* ligation of transforming DNA to mitochondrial DNA sequences. *Mol Cell Biol* 1993, 13: 2697–2705
48. Longtine MS, Mckenzie III A, Demarini DJ, Shah NG, Wach A, Brachat A, Philippsen P, ***et al.*** Additional modules for versatile and economical PCR-based gene deletion and modification in *Saccharomyces cerevisiae*. *Yeast* 1998, 14: 953–961
49. Howson R, Huh W-, Ghaemmaghami S, Falvo JV, Bower K, Belle A, Dephoure N, ***et al.*** Construction, verification and experimental use of two epitope-tagged collections of budding yeast strains. *Comp Funct Genom* 2005, 6: 2–16
50. Tapia H, Morano KA, Glick BS. Hsp90 nuclear accumulation in quiescence is linked to chaperone function and spore development in yeast. *Mol Biol Cell* 2010, 21: 63–72
51. Molliex A, Temirov J, Lee J, Coughlin M, Kanagaraj AP, Kim HJ, Mittag T, ***et al.*** Phase separation by low complexity domains promotes stress granule assembly and drives pathological fibrillization. *Cell* 2015, 163: 123–133
52. Nott TJ, Petsalaki E, Farber P, Jervis D, Fussner E, Plochowietz A, Craggs TD, ***et al.*** Phase transition of a disordered nuage protein generates environmentally responsive membraneless organelles. *Mol Cell* 2015, 57: 936–947
53. Hipp MS, Kasturi P, Hartl FU. The proteostasis network and its decline in ageing. *Nat Rev Mol Cell Biol* 2019, 20: 421–435
54. Hubstenberger A, Courel M, Bénard M, Souquere S, Ernoult-Lange M, Chouaib R, Yi Z, ***et al.*** P-Body purification reveals the condensation of repressed mRNA regulons. *Mol Cell* 2017, 68: 144–157.e5
55. Yang P, Mathieu C, Kolaitis RM, Zhang P, Messing J, Yurtsever U, Yang Z, ***et al.*** G3BP1 is a tunable switch that triggers phase separation to assemble stress granules. *Cell* 2020, 181: 325–345.e28
56. Hofmann S, Kedersha N, Anderson P, Ivanov P. Molecular mechanisms of stress granule assembly and disassembly. *Biochim Biophys Acta* 2021, 1868: 118876
57. Kolhe JA, Babu NL, Freeman BC. The Hsp90 molecular chaperone governs client proteins by targeting intrinsically disordered regions. *Mol Cell* 2023, 83: 2035–2044.e7
58. Girstmair H, Tippel F, Lopez A, Tych K, Stein F, Haberkant P, Schmid PWN, ***et al.*** The Hsp90 isoforms from *S. cerevisiae* differ in structure, function and client range. *Nat Commun* 2019, 10: 3626
59. Riedl S, Bilgen E, Agam G, Hirvonen V, Jussupow A, Tippl F, Riedl M, ***et al.*** Evolution of the conformational dynamics of the molecular chaperone Hsp90. *Nat Commun* 2024, 15: 8627